JM PAPERS

Elevated low-frequency free-stream vortical disturbances eliminate boundary-layer separation

Dongdong Xu[1,2] and Xuesong Wu[3,2],†

[1]Department of Mechanics, Tianjin University, Tianjin 300072, PR China

[2]Department of Mathematics, Imperial College London, 180 Queen's Gate, London SW7 2AZ, UK

[3]School of Mechanical Engineering, Nantong University, Nantong 226019, PR China

A steady two-dimensional boundary layer subject to an adverse streamwise pressure gradient usually separates. In this paper, we investigate how free-stream vortical disturbances (FSVD) of moderate level prevent the separation in such a boundary layer over a plate or concave wall. The focus is on physically realisable FSVD with sufficiently long wavelength (low frequency) as they have the most significant impact on the boundary layer. The FSVD intensity ϵ is taken to be small but nevertheless strong enough that the streaks or Görtler vortices generated in the boundary layer are fully nonlinear and can alter the mean-flow profile by an order-one amount. The excitation and evolution of streaks and Görtler vortices are governed by the nonlinear unsteady boundary-region equations supplemented by appropriate initial (upstream) and boundary (far-field) conditions, which describe appropriately the action of FSVD on the boundary layer. The flow variables are decomposed into two parts: the steady spanwise-averaged and the unsteady or spanwise-varying components. These two parts are coupled and are computed simultaneously. Numerical results show that the separation is eliminated when the FSVD level exceeds a critical intensity ϵ_c. It is inferred that the strong nonlinear mean-flow distortion associated with the nonlinear streaks or Görtler vortices prevents the separation. The critical FSVD intensity ϵ_c depends on the streamwise curvature, the pressure gradient and the frequency of FSVD. The value of ϵ_c decreases significantly with the Görtler number, indicating that concave curvature inhibits separation. A higher ϵ_c is required to prevent the separation in the case of stronger adverse pressure gradient. Interestingly, unsteady FSVD with low frequencies are found to be more effective than steady ones in suppressing the separation.

Key words: boundary layer separation, boundary layer receptivity, boundary layer stability

† Email address for correspondence: x.wu@ic.ac.uk

1. Introduction

A steady laminar boundary layer over a smooth surface separates when it encounters a strong enough adverse pressure gradient. This induces a so-called laminar separation bubble (LSB), the flow in which may undergo laminar–turbulent transition. LSBs are distinguished as short and long ones, based on the bubble length relative to the chord length of an aerofoil (Owen & Klanfer 1953), or whether their impact on the pressure distribution is local or global (Tani 1964). LSBs appear in many practical flows such as those around aerofoils and turbine blades, and have a remarkable effect upon aerodynamic behaviours, causing performance penalties, such as drag increase or even stall. It is therefore necessary to predict, reduce and if possible prevent, LSBs. This effort can be aided by investigating the relevant physical mechanisms generating and suppressing the separation, which are still not completely understood due to their complexity.

The physical nature of steady laminar flows over solid boundaries at high Reynolds numbers can be explained and described by the classical boundary-layer theory (Prandtl 1904), which asserts that the viscous effect plays a leading-order role in a thin layer near the surface while being negligible elsewhere. The inviscid part of the flow can be considered first to obtain the slip velocity and pressure gradient, which drive the viscous flow in the thin boundary layer. The equations governing the viscous flow are parabolic and hence can be solved using efficient marching methods to calculate the quantities of aerodynamic interest, e.g. the drag, when the boundary layer does not separate. However, the downstream marching becomes problematic when the skin friction approaches zero (Cebeci & Cousteix 2005), which signals separation. A detailed analysis of the asymptotic behaviour near a point of vanishing skin friction, x_s, showed that the skin friction τ and the boundary-layer thickness δ in general behave like $\tau = O((x_s - x)^{1/2})$ and $\delta = O((x_s - x)^{1/2})$ as $x \to x_s^-$, and accordingly the viscous effect induces a transpiration velocity $v_\infty = O((x_s - x)^{-1/2})$ (Goldstein 1948); this set of results is referred to as Goldstein singularity. In the classical boundary-layer theory, the inviscid flow is not influenced at leading order by the displacement effect of the viscous boundary-layer flow. That hierarchical structure no longer holds, and the theory loses its validity when separation occurs due to the large displacement-induced transpiration velocity. Stewartson (1970) included the boundary-layer displacement effect on the outer inviscid flow at leading order, but unfortunately a separation singularity of Goldstein type cannot be eliminated solely by this local viscous–inviscid interaction. In this case, the separation bubble is actually large enough to disrupt the inviscid flow at large distances upstream. The mathematical description for the latter must instead account for the global effect of the grossly separated boundary layer (Sychev 1972). The interactive boundary-layer method, which is a heuristic finite-Reynolds-number reformulation of the high-Reynolds-number asymptotic theory, has also been employed to study the separation phenomenon (Carter & Wornom 1975; Veldman 1981; Hsiao & Pauley 1994).

Typically, the degree of the adverse pressure gradient is controlled by a parameter, e.g. the angle of attack of an aerofoil. When the parameter reaches a critical value, the skin friction τ predicted by the classical boundary-layer equations vanishes at x_s, in the vicinity of which τ is weakly singular (i.e. non-analytic), $\tau \sim |x - x_s|$, and a short separation bubble forms (Ruban 1981). This is the so-called marginal separation. Ruban (1982) and Stewartson, Smith & Kaups (1982) formulated a high-Reynolds-number asymptotic theory describing a marginal separation. In this theory, the displacement effect of the viscous boundary layer induces a pressure perturbation in the outer inviscid flow, which also acts on the viscous part of the flow. This local inviscid–viscous interaction eliminates the weak singularity representing the flow on the verge of separation even when the controlling

parameter, e.g. the angle of attack, exceeds the critical value. Local inhomogeneities influence marginal separation. An isolated three-dimensional surface-mounted obstacle, in the form of a sufficiently high slender hump, is an effective means to force reattachment of an oncoming two-dimensional marginally separating boundary layer. Servini, Smith & Rothmayer (2017, 2018) studied the impact of a two-dimensional dynamic roughness element on a separating boundary layer. Recently, Karp & Hack (2020) showed, by numerical simulations, reduction of separation bubble size by the so-called optimal disturbances. The optimal three-dimensional disturbances were calculated by a numerical optimisation procedure according to chosen objective functions, but it remains unclear how such perturbations could be produced within the boundary layer at the required streamwise location by a viable actuator in laboratory.

1.1. *Laminar separation and instability*

Laminar boundary-layer separation and transition to turbulence, two of the most subtle phenomena in fluid mechanics, are often closely related because a boundary layer that is separated or undergoing separation becomes unstable, while at the same time the instabilities and resulting transition impact the separation. The topic has received much attention. Earlier studies were reviewed by Dovgal, Kozlov & Michalke (1994), and much progress has been made since. It is well-known that a two-dimensional or weakly three-dimensional essentially inviscid Kelvin–Helmholtz (K–H) instability operates and dominates in the fore portion of a LSB, but viscous Tollmien–Schlichting (T–S) instability may occur upstream of the separation point if the Reynolds number is large enough (Häggmark, Bakchinov & Alfredsson 2000; Marxen *et al.* 2003), in which case a K–H instability wave may be considered as the continuation of an upstream T–S mode (Rist & Maucher 2002; Diwan & Ramesh 2009; Marxen, Lang & Rist 2012). In the well-separated and reattached regions, the streamwise gradient of the transverse velocity of the base flow, $\partial V_B/\partial x$, could be significant, and since it plays a similar role to the familiar centrifugal force induced by wall curvature, a centrifugal instability may operate, leading to spatial growth of steady or low-frequency perturbations akin to Görtler vortices (Marxen *et al.* 2009; Marxen & Henningson 2011). By means of controlled excitation in experiments (Watmuff 1999; Kurelek, Lambert & Yarusevych 2016) and direct numerical simulation (DNS) (Marxen *et al.* 2003, Marxen, Rist & Wagner 2004; Marxen, Lang & Rist 2013), it has been demonstrated that, through nonlinear development, K–H modes roll up, forming predominantly spanwise vortices, which undergo spanwise modulation (Michelis, Yarusevych & Kotsonis 2018). With harmonic forcing at appropriate frequencies, the size of the LSB is reduced because the resulting earlier transition to turbulence shifts the reattachment point upstream, and in certain cases the separation point moves downstream as well (Rist & Augustin 2006; Yarusevych & Kotsonis 2017). Impulsive forcing was found to cause the bubble to shrink first, followed by elongation (bursting) (Michelis, Yarusevych & Kotsonis 2017).

Within a LSB, two types of primary absolute instabilities were identified: one is supported by the mean flow with a sufficiently strong reverse flow (Hammond & Redekopp 1998; Rist & Maucher 2002; Embacher & Fasel 2014), while the other is a bi-global 'elliptic' or 'centrifugal' instability with the mode being three-dimensional and trapped in the recirculation zone (Theofilis, Hein & Dallmann 2000; Gallaire, Marquillie & Ehrenstein 2007; Rodríguez & Theofilis 2010); here, the instabilities are deemed 'absolute' because they manifest as amplification of persistent disturbances in space without being swept away, which is a more general notion than the usual absolute instability established for a parallel or locally parallel flow according to a zero group velocity. These instabilities

may lead to self-sustained oscillations and three-dimensionalisation of a LSB respectively when the reverse flow exceeds the respective thresholds (Rodríguez, Gennaro & Juniper 2013). The height and length of the LSB may also be important factors controlling the instabilities, but a recent study suggests that the onset of the absolute instability of the first type is associated with the inflection point of the mean velocity profile just moving into the recirculation zone (Avanci, Rodríguez & Alves 2019). Furthermore, new states emerging from the primary instabilities may be susceptible to secondary instabilities. The time-periodic base flow associated with the saturated K–H rollers undergoes secondary high-frequency absolute instability, through which the rollers break down into small-scale turbulence (Alam & Sandham 2000; Jones, Sandberg & Sandham 2008; Embacher & Fasel 2014). Interestingly, the time-periodic state appears to exhibit also a steady or low-frequency secondary instability, leading to quasi-exponential spatial amplification of streak-like disturbances (Hosseinverdi & Fasel 2018, 2019). The latest work of Rodríguez, Gennaro & Souza (2021) shows that the nonlinear saturated state originated from the bi-global three-dimensional stationary instability may support secondary absolute instability to time-dependent perturbations.

1.2. *Role of free-stream disturbances*

In practical applications, naturally present external disturbances may excite convectively unstable modes, thereby impacting the separation. The effects of free-stream acoustic waves have been studied extensively; see Dovgal *et al.* (1994) for relevant references. Free-stream turbulence (FST) has a significant influence on LSBs also. As the FST level Tu is increased, the length of the LSB reduces, primarily because the mean reattachment point shifts upstream (Istvan, Kurelek & Yarusevych 2017; Simoni *et al.* 2017), but appreciable downstream movement of the mean separation position has also been observed (O'meara & Mueller 1987; Olson *et al.* 2013; Istvan & Yarusevych 2018). The height of the LSB is reduced as well. When Tu exceeds a threshold of approximately 2 %, the separation may be eliminated completely (Simoni *et al.* 2016, 2017; Istvan & Yarusevych 2018), and remarkably this occurs with the flow remaining laminar (Simoni *et al.* 2016). The precise threshold Tu was found to depend on the Reynolds number and flow configuration (Simoni *et al.* 2017). DNS broadly confirmed the experimental finding that FST inhibits the size of the LSB (Wissink & Rodi 2006; McAuliffe & Yaras 2010; Balzer & Fasel 2016). At low and moderate Tu levels, K–H modes are excited, undergo roll-up and spanwise modulation and break down into small-scale turbulence. At high levels, low-frequency components in FST entrain into the boundary layer to form streaks, which influence separation and/or reattachment processes with (McAuliffe & Yaras 2010) or without causing bypass transition (Balzer & Fasel 2016); in the latter case the streaks modulate the shear layer and hence the K–H instability (Coull & Hodson 2011). Hosseinverdi & Fasel (2018) performed DNS of separation and transition in the presence of both controlled harmonic excitation and FST that is synthesised mathematically. The harmonic forcing, which is fairly strong, reduces the LSB length significantly (to approximately 1/4 of that in the uncontrolled case). FST at very low levels influences neither separation nor reattachment. Nevertheless, it induces streaks of appreciable amplitude, which undergo exponential amplification in the LSB. Transition occurs earlier than when FST is absent but remains downstream of the reattachment. Without harmonic forcing, even very weak FST was able to influence reattachment. Beyond a certain level of FST, streaks render transition to take place before reattachment, and the latter shifts upstream as a result, leading to reduction of the LSB length and height (Hosseinverdi & Fasel 2019). For all the FST levels up to 3 %, a LSB persists with the mean separation point remaining fixed.

It was suggested that the absolute instability due to the spanwise modulation of the shear layer by streaks of sufficient amplitude may be operative, causing earlier transition and reattachment (Rodríguez *et al.* 2021).

FST can influence separation through triggering convectively unstable modes via receptivity (which remains poorly understood), or more directly by altering the overall mean flow. The latter scenario will be the focus of the present study. In either of the mechanisms, the process of FST entering, or interacting with, the separated or separating boundary layer is of fundamental importance, and adequate understanding of this is a prerequisite for an accurate prediction of separation and transition.

Leib, Wundrow & Goldstein (1999) presented a large-Reynolds-number theory to describe how small-amplitude, low-frequency (long-wavelength) free-stream vortical disturbances (FSVD) are entrained into the boundary layer over a flat plate. They assumed that the turbulent Reynolds number $r_t = \epsilon R_\Lambda \ll 1$, where ϵ measures the FSVD intensity and R_Λ is the Reynolds number based on the spanwise wavelength Λ. A significant finding is that $O(\epsilon)$ long-wavelength FSVD generate streaks with $O(\epsilon R_\Lambda)$ amplitude in the boundary layer. The work of Leib *et al.* (1999) was extended by Wu, Zhao & Luo (2011) to investigate excitation of Görtler vortices in the boundary layer over a concave wall. On the other hand, Ricco, Luo & Wu (2011) studied the case where FSVD are of moderate intensity with $r_t = O(1)$, for which the induced streaks may completely alter the base flow. The resulting streaky boundary layer supports inviscid instability before the onset of T–S instability. Marensi, Ricco & Wu (2017) considered nonlinear FSVD-induced streaks in compressible boundary layers. These studies analysed the boundary-layer response to the FSVD starting from the region close to the leading edge, and followed its subsequent development. FSVD impact the boundary layer not only through the initial condition but also by the far-field boundary condition. At the same time, the displacement effect of the viscous streaky motion in the boundary layer affects the FSVD at the outer edge of the boundary layer.

It should be noted that the initial and far-field conditions in the studies mentioned above (Leib *et al.* 1999; Ricco *et al.* 2011; Marensi *et al.* 2017) are not continuous spectra of the Orr–Sommerfeld (O–S) or Squire equations (Grosch & Salwen 1978). Because the eigenfunction of a continuous spectrum does not vanish, and its phase speed is nearly equal to the free-stream velocity, it has been proposed that the continuous spectra may be used as the inlet and far-field conditions, representing the vortical disturbances present in the free stream as well as entrained into the boundary layer (Jacobs & Durbin 2001), and this practice has been followed by many researchers in their DNS of bypass transition, receptivity (Durbin & Wu 2007) and separation (see below). The appropriateness of these practices was called into question by Dong & Wu (2013), who showed that the entrainment of physical FSVD into the boundary layer is influenced at leading order by the non-parallel-flow effect, while this effect is completely ignored in the continuous modes, leading to a number of non-physical features. Their work was for incompressible boundary layers and for FSVD with a characteristic wavelength of the order of the local boundary-layer thickness, and was subsequently extended to compressible boundary layers and to FSVD with an even shorter wavelength, which is comparable to the width of the so-called edge layer (Wu & Dong 2016).

Xu, Zhang & Wu (2017) extended the work of Ricco *et al.* (2011) by including the centrifugal effect. The induced disturbances by FSVD undergo nonlinear saturation and eventually evolve into Görtler vortices, the secondary instability of which was further analysed. The predicted nonlinear development of Görtler vortices was found to be in good agreement with experiments. Xu, Liu & Wu (2020) developed the theory for the nonlinear excitation of streaks or Görtler vortices by FSVD in an attached boundary layer

with a streamwise pressure gradient. In both of the above studies, the theories captured an abrupt change of the skin friction, which is induced by nonlinear vortices. The mean-flow distortion would increase the skin friction at all spanwise locations, whereas the influence of harmonics on the skin friction depends on the spanwise location.

1.3. *Objectives of the present study*

The boundary-layer flows studied by Ricco *et al.* (2011) and Xu *et al.* (2017, 2020) are subject to zero or a moderate adverse pressure gradient and thus remain attached. Separation would take place with a further increase of the adverse pressure gradient. By imposing elevated FSVD, the mean skin friction may rise significantly and hence the boundary layer might be prevented from separating. In the present paper, we will investigate this direct mechanism, which is simpler and perhaps more fundamental than the indirect one involving excitation of short-wavelength instability modes. As was mentioned above, experiments and DNS showed that streaks impact the reattachment by changing the mean-flow characteristics. It is not unreasonable to expect that streaks could influence separation in a similar way. A recent numerical study indicated that steady three-dimensional optimal perturbations, which exhibit the character of streaks, may reduce the LSB size by causing a mean-flow distortion (Karp & Hack 2020). A case for the direct effect of FSVD may be made by discussing its role in separation with respect to that of instabilities and the associated transition. Relevant instability include boundary-layer instability in the pre-separation region, secondary instability of the FSVD induced streaky flow and shear-layer instability when a LSB is present. Since these instabilities are convective in nature and have relatively short characteristic wavelengths, the modes need to be excited by viable receptivity processes, which require free-stream disturbances in the relatively high-frequency bands as well as surface inhomogeneity (e.g. roughness) over short scales. It is in principle possible to weaken the receptivity, e.g. by maintaining an as smooth as possible surface and/or by damping the relevant spectra in the free-stream disturbances, whereby the amplitudes of instability modes may be made sufficiently low so that transition, although taking place, has a minimal effect on the separation. It is thus meaningful to explore whether separation could be eliminated without the action of short-wavelength instabilities or resulting turbulence. Experiments showed that FST of sufficient intensity can completely eliminate separation with the flow remaining laminar (Simoni *et al.* 2016, 2017; Zilli, Sutton & Lavoie 2017). A nearly complete suppression of LSB at a rather moderate FST level was also observed (Istvan & Yarusevych 2018). The direct mechanism of FSVD to be investigated would be relevant at least to separation close to being marginal, since in that case the LSB is short and hence the amplification of instability modes in the bubble would be rather limited while the required FSVD intensity is rather low. Furthermore, Kalter & Fernholz (2001) observed that in an already turbulent boundary-layer FST also reduces the size of a separation bubble and may even eliminate it, suggesting that a mechanism alternative to excitation of instability and transition might be at work. A candidate might be the direct modification of the mean flow due to the streaks altering the Reynolds stresses since significant alterations were clearly demonstrated in the measurements. Even in the case of instability modes being excited, the effect on separation is exerted through the mean-flow distortion, generated by nonlinear modal interactions (Marxen & Rist 2010). On the other hand, steady free-stream vorticity aligned to the streamwise direction or normal to the leading edge may induce separation in a nominally zero-pressure-gradient boundary layer (Goldstein, Leib & Cowley 1992; Goldstein & Leib 1993).

Obviously, it is of primary importance in theoretical and numerical modelling to specify physically realisable perturbations and the corresponding inlet conditions if the computation is performed in a truncated domain. A number of DNS (e.g. Balzer & Fasel 2016; Hosseinverdi & Fasel 2018, 2019) represented free-stream and inlet disturbances by continuous spectra of the O–S/Squire operators, which are shown to be non-physical (Dong & Wu 2013; Wu & Dong 2016). On the other hand, McAuliffe & Yaras (2010) employed a large domain extending to the uniform flow upstream, where suitable perturbations can be specified. Simulations using the two treatments capture the overall effects of FST qualitatively, but significant differences exist. With FST and inlet conditions being specified in terms of continuous spectra, sizeable separation bubble persisted at FST levels up to 3 %, whereas DNS using appropriate FST showed that the separation bubble becomes rather benign at a lower level of 1.45 %, and a complete elimination of the separation bubble is possible beyond a threshold level of approximately 2 % as may be expected according to experimental observations (Simoni *et al.* 2016, 2017; Istvan & Yarusevych 2018). It may be inferred that free-stream and inlet disturbances represented by continuous spectra, and indeed more-or-less arbitrary steady or low-frequency disturbances, can generate boundary-layer perturbations bearing gross signatures of streaks or Klebanoff modes, which influence separation. Calculations using those disturbances may capture the phenomena quantitatively. However, for quantitatively correct predictions, it is important to impose physically realizable FSVD as well as the consistent initial and boundary conditions.

The mechanisms of FST preventing separation are not all entirely clear. In the present paper, we consider a possible mechanism by which physically realisable FSVD eliminate separation through modifying the mean-flow characteristics, and a theoretical description will be presented, which allows us to predict the threshold FSVD intensity required for the removal of the separation. The present study builds on our previous work (Xu *et al.* 2020), which provides the appropriate upstream and far-field boundary conditions describing quantitatively the impact of low-frequency components in FST on the boundary layer. The presence of an adverse pressure means that the inviscid flow is necessarily non-uniform, and so the oncoming FSVD undergo distortion before entering the boundary layer. This important physical process as well as the leading-order non-parallelism are ignored in continuous spectrum representation, but are accounted for properly in our theory.

The rest of the paper is organised as follows. In § 2, we adapt the theory (i.e. the initial-boundary-value problem) describing the excitation and nonlinear evolution of streaks or Görtler vortices by FSVD (Xu *et al.* 2020) to boundary layers that would separate if FSVD were absent. The total flow field is split into the steady spanwise-averaged part and the unsteady or spanwise-varying parts. They are governed by a system of coupled equations. In § 3, we describe the numerical procedure to solve this system. The results for representative pressure gradients are presented in § 4; those of particular interest are the threshold FSVD intensity for suppressing separation and its dependence on relevant parameters such as the mean pressure gradient, wall curvature and the frequency of FSVD. The conclusions and implications of the results are discussed in § 5.

2. Problem formulation

2.1. *Scaling and governing equations*

The flow of interest is an incompressible boundary layer that develops over a semi-infinite flat or concave wall, and is subject to an adverse pressure gradient. The setting is similar to laboratory experiments, where a pressure gradient is created by a ceiling

of a suitable contour over the wall, starting from the leading edge, or some distance downstream/upstream of it. For a concave wall, the characteristic radius of curvature is r_0^*. Small-amplitude vortical fluctuations, with a characteristic length scale Λ, are imposed on the uniform oncoming flow far upstream. They are taken to be of a simple form: a pair of Fourier components with the same frequency but opposite dimensional spanwise wavenumbers $\pm k_3^*$. We focus on disturbances with low frequency, or equivalently long streamwise wavelength $2\pi/k_1^* \gg \Lambda$, to which the boundary layer is most receptive, where k_1^* is the dimensional streamwise wavenumber. Our previous work indicates that disturbances of the assumed form are capable of elucidating the key physical mechanism of transition (Xu *et al.* 2017).

The flow is to be described in a curvilinear coordinate system (x^*, y^*, z^*), with the origin at the leading edge of the wall, where x^* and y^* are in the directions along and normal to the wall, respectively, and z^* is along the span. Taking Λ and U_∞ as the reference length and velocity, respectively, we introduce non-dimensional coordinates and time variable,

$$(x, y, z) = (x^*, y^*, z^*)/\Lambda, \quad t = U_\infty t^*/\Lambda, \tag{2.1a,b}$$

where t^* is the dimensional time. The Reynolds number is defined as

$$R_\Lambda = U_\infty \Lambda/\nu, \tag{2.2}$$

where ν is the kinematic viscosity. We assume that $R_\Lambda \gg 1$ so that viscous effects are confined to a thin layer near the surface, and the flow physics can be analysed using the technique of matched asymptotic expansion and multi-scale method.

The long-wavelength (low-frequency) FSVD and the induced streaks are described by the slow streamwise and time variables, introduced as,

$$\hat{x} = x/R_\Lambda, \quad \hat{\tau} = t/R_\Lambda. \tag{2.3a,b}$$

The disturbances in the far upstream region are passively advected by the uniform background flow. It follows that the total velocity field, normalised by U_∞, can be written as $(u^*, v^*, w^*)/U_\infty = (1, 0, 0) + \tilde{\boldsymbol{u}}_\infty$, with the disturbance velocity $\tilde{\boldsymbol{u}}_\infty$ taking the form

$$\tilde{\boldsymbol{u}}_\infty = \epsilon \boldsymbol{u}_\infty(\hat{x} - \hat{\tau}, y, z) = \epsilon(\widehat{\boldsymbol{u}}_+^\infty \, e^{ik_3 z} + \widehat{\boldsymbol{u}}_-^\infty \, e^{-ik_3 z}) \exp[i\hat{k}_1(\hat{x} - \hat{\tau}) + ik_2 y] + \text{c.c.}, \tag{2.4}$$

where $\epsilon \ll 1$ measures the disturbance intensity, $\hat{\boldsymbol{u}}_\pm^\infty = \{\hat{u}_{1,\pm}^\infty, \hat{u}_{2,\pm}^\infty, \hat{u}_{3,\pm}^\infty\} = O(1)$ is the scaled velocity, $\boldsymbol{k} = \{k_1, k_2, k_3\}$ the wavenumber vector and $\hat{k}_1 = k_1 R_\Lambda = O(1)$. The continuity condition implies that

$$k_1 \hat{u}_{1,\pm}^\infty + k_2 \hat{u}_{2,\pm}^\infty \pm k_3 \hat{u}_{3,\pm}^\infty = 0. \tag{2.5}$$

Here, for simplicity FSVD are represented by a pair of oblique Fourier modes, but it is straightforward to extend the ensuing analysis and calculations to a continuum of components that are representative of true FST, as was done in Zhang *et al.* (2011).

The turbulent Reynolds number is defined as (Leib *et al.* 1999; WZL),

$$r_t \equiv \epsilon R_\Lambda = O(1). \tag{2.6}$$

As was shown by Leib *et al.* (1999) for the flat-plate case and by Xu *et al.* (2017, 2020) for concave walls, the ensuing flow evolves through four asymptotic regimes as is illustrated in figure 1. The inviscid region I has $O(\Lambda)$ size in all three directions, and the disturbance there is governed by the linear rapid-distortion theory (Goldstein 1978; Goldstein & Durbin 1980). Beneath region I is the boundary layer (region II) with a
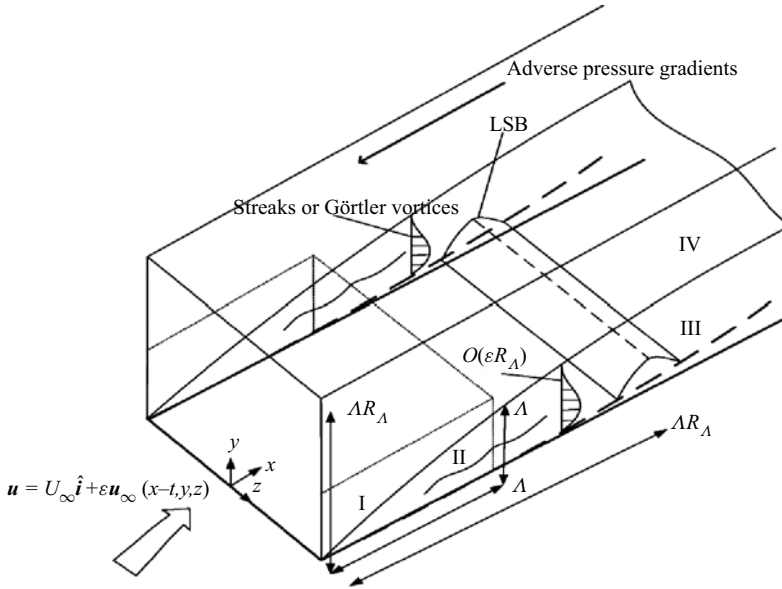
Figure 1. Schematic illustration of the physical problem and asymptotic structure.

thickness of $O(R_\Lambda^{-1/2}\Lambda)$, where viscosity plays a leading-order role but the centrifugal force is negligible. A quasi-two-dimensional and a three-dimensional disturbance are driven by the streamwise and spanwise components of the FSVD, respectively. Downstream in region III, which has an $O(\Lambda)$ thickness, the three-dimensional disturbance driven by the FSVD develops into streaks or Görtler vortices, and is governed by the nonlinear unsteady boundary-region equations (NUBRE). It should be noted that, in the present work, the boundary layer is subject to an adverse pressure gradient, which may induce a steady two-dimensional LSB in region III. Above region III is an outer region IV with an $O(R_\Lambda\Lambda)$ thickness, the disturbance in which interacts with that in region III.

As in Xu *et al.* (2020), an adverse pressure gradient can be created by placing the plate in an expanding channel. The expansion ratio of the channel is

$$\sigma_c = a^*/b^* = O(1), \tag{2.7}$$

where a^* and b^* are the transverse dimensions of the upstream and downstream flow passages, and the mean velocities there are denoted by U_+ and U_- respectively. The length of streamwise non-uniformity is $l^* = O(a^*) = O(b^*)$. The disturbance near the leading edge can be determined by the rapid-distortion theory.

In region III, the streaks or Görtler vortices are fully developed, and their streamwise velocity has a magnitude greater than the normal and spanwise velocities by a factor of $O(R_\Lambda)$, while the pressure normalised by ρU_∞^2 is of $O(1)$ for the steady base flow, but of $O(R_\Lambda^{-2})$ for the perturbation, where ρ is the fluid density. Therefore, we can write the velocity and pressure fields, (u^*, v^*, w^*) and p^*, as

$$(u^*, v^*, w^*)/U_\infty = (u, R_\Lambda^{-1}v, R_\Lambda^{-1}w), \quad p^*/(\rho U_\infty^2) = P_B + R_\Lambda^{-2}p, \tag{2.8a,b}$$

where P_B is the steady mean pressure associated with the steady inviscid outer flow. Substitution of (2.3a,b) and (2.8a,b) with the Lamè coefficients, $h_1 = (r_0^* - y^*)/r_0^*$, $h_2 = 1$ and $h_3 = 1$, into the Navier–Stokes (N–S) equations gives, at leading order, the equations

920 A14-9

for the rescaled velocity $\boldsymbol{u} \equiv (u, v, w)$ and pressure p (Hall 1988),

$$\boldsymbol{\nabla} \cdot \boldsymbol{u} = 0, \quad \boldsymbol{u}_{\hat{\tau}} + (\boldsymbol{u} \cdot \boldsymbol{\nabla})\boldsymbol{u} + G_\Lambda \chi_B u^2 \boldsymbol{j} = (-P_{B\hat{x}}, -p_y, -p_z) + (\partial_{yy}^2 + \partial_{zz}^2)\boldsymbol{u}, \quad (2.9)$$

where $\boldsymbol{j}$ is the unit vector in the wall-normal direction, and G_Λ is the global Görtler number, defined as

$$G_\Lambda = R_\Lambda^2 \Lambda / r_0^*. \quad (2.10)$$

The term containing G_Λ in (2.9) reflects the essential influence of the wall curvature, and $\chi_B(\hat{x})$ is the scaled local radius of wall curvature. The term $P_{B\hat{x}}(\hat{x}) = -U_e(\hat{x})U_e'(\hat{x})$ is the streamwise pressure gradient with $U_e(\hat{x})$ being the inviscid streamwise slip velocity of the steady flow, and the prime denoting the differentiation with respect to $\hat{x}$.

In the previous work Xu *et al.* (2017, 2020), the total flow field in region III is decomposed as a sum of the unperturbed base flow and the FSVD-induced perturbation. This decomposition would be inappropriate in the presence of a strong adverse pressure gradient that induces separation because the solution for the former terminates at a Goldstein singularity. In order to avoid this dead end, and also to provide insight into the mechanism of eliminating separation, in the present study the flow is decomposed instead as a sum of two parts: (a) the steady spanwise-averaged components, and (b) the steady and unsteady spanwise-varying components as well as the unsteady spanwise uniform component, namely

$$\begin{aligned}\{u, v, w, p\} = {} &\{U_B(\hat{x}, \eta), V_B(\hat{x}, \eta), W_B(\hat{x}, \eta), P_B(\hat{x})\} \\ &+ \{\hat{u}(\hat{x}, \eta, z, \hat{\tau}), \hat{v}(\hat{x}, \eta, z, \hat{\tau}), \hat{w}(\hat{x}, \eta, z, \hat{\tau}), \hat{p}(\hat{x}, \eta, z, \hat{\tau})\}, \quad (2.11)\end{aligned}$$

where the second part has zero spanwise average for steady FSVD, but also contains an unsteady spanwise uniform component if FSVD are unsteady. The present decomposition is in line with the practice in DNS and experiments, where the steady and spanwise uniform part of the flow is extracted from the instantaneous data by time and spanwise averaging in order to characterise the mean property of the separation (Marxen & Henningson 2011; Balzer & Fasel 2016; Simoni *et al.* 2016, 2017; Yarusevych & Kotsonis 2017). The resulting formulation will enable us to show that the boundary layer is attached provided $\epsilon > \epsilon_c$, where the attached flow as well as ϵ_c, the critical FSVD intensity to eliminate the separation, can be calculated.

With (2.11), the nonlinear terms in (2.9) are accordingly decomposed as

$$-(\hat{\boldsymbol{u}} \cdot \boldsymbol{\nabla})\hat{\boldsymbol{u}} - G_\Lambda \chi \hat{u}^2 \boldsymbol{j} = (Q_1, Q_2, Q_3)(\hat{x}, y) + (\hat{q}_1, \hat{q}_2, \hat{q}_3)(\hat{x}, y, z, \hat{\tau}). \quad (2.12)$$

Substituting (2.11) into (2.9) and noting (2.12), we obtain the coupled system,

$$U_{B\hat{x}} + V_{By} = 0, \quad \bar{D}U_B = P_{B\hat{x}} + Q_1, \quad \bar{D}W_B = Q_3, \quad (2.13a\text{–}c)$$

and

$$\left.\begin{aligned}\hat{u}_{\hat{x}} + \hat{v}_y + \hat{w}_z &= 0, \\ D\hat{u} - U_{B\hat{x}}\hat{u} - U_{By}\hat{v} &= \hat{q}_1, \\ D\hat{v} - V_{B\hat{x}}\hat{u} - V_{By}\hat{v} - 2G_\Lambda \chi_B U_B \hat{u} - \hat{p}_y &= \hat{q}_2, \\ D\hat{w} - W_{B\hat{x}}\hat{u} - W_{By}\hat{v} - \hat{p}_z &= \hat{q}_3, \end{aligned}\right\} \quad (2.14)$$

where

$$\bar{D} = \frac{\partial^2}{\partial y^2} - U_B \frac{\partial}{\partial \hat{x}} - V_B \frac{\partial}{\partial y}, \quad (2.15)$$

$$D = \left(\frac{\partial^2}{\partial y^2} + \frac{\partial^2}{\partial z^2}\right) - \frac{\partial}{\partial \hat{\tau}} - U_B \frac{\partial}{\partial \hat{x}} - V_B \frac{\partial}{\partial y} - W_B \frac{\partial}{\partial z}. \quad (2.16)$$

920 A14-10

The operator D accounts for the unsteadiness and the viscous diffusion in the $y - z$ plane, as well as the convection by the spanwise-averaged flow field. The governing equations (2.13a–c)–(2.14) are almost the same as (4.2)–(4.3) in Wundrow & Goldstein (2001), respectively, but here we include the streamwise curvature and pressure gradient. Note that the spanwise-averaged flow is driven not only by the pressure gradient, but also by the Reynolds stresses of the spanwise-varying part. As a result, a spanwise velocity W_B is present in general. On the other hand, the spanwise-averaged part influences the spanwise-varying part through advection, as is reflected in the operator D. Such a coupling leads to elimination of the separation when FSVD are strong enough. Note that (2.13a–c), which govern the steady spanwise-averaged mean flow, remain the same for both steady and unsteady FSVD, implying that the mechanism of eliminating the separation is the same, namely, through the time- and spanwise-averaged Reynolds stresses.

The solution is of course not self-similar, but for numerical computations, it is advantageous to use the similarity-like variable η, defined as

$$\eta = y/s \quad \text{with } s = \sqrt{2\hat{x}/U_e}. \tag{2.17}$$

Despite the fact that FSVD are represented by a pair of oblique Fourier components, in the present nonlinear regime the spanwise-varying disturbance consists of all harmonics (plus the unsteady spanwise uniform part if FSVD are unsteady), and can be expressed as

$$(\hat{u}, \hat{v}, \hat{w}, \hat{p}) = r_t \sum_{|m|+|n| \neq 0} (s^2 \hat{u}_{m,n}(\hat{x}, \eta), s\hat{v}_{m,n}(\hat{x}, \eta), \hat{w}_{m,n}(\hat{x}, \eta)/k_3, \hat{p}_{m,n}(\hat{x}, \eta)) E_{mn}, \tag{2.18}$$

where $E_{mn} = \exp(-im\hat{k}_1\hat{\tau} + ink_3 z)$, and the factor s^2 in the streamwise velocity is introduced to offset the small divisor in numerical computations. As the physical quantities are real, the Fourier coefficients are Hermitian, $\hat{q}_{-m,-n} = (\hat{q}_{m,n})_{cc}$, where $\hat{q}$ stands for any of $\{\hat{u}_{m,n}, \hat{v}_{m,n}, \hat{w}_{m,n}, \hat{p}_{m,n}\}$, and the subscript cc indicates the complex conjugate. Substituting (2.18) into (2.14), we obtain the equations for the Fourier coefficients

a. the continuity equation

$$2\mathcal{B}_v \hat{u}_{m,n} + s^2 \frac{\partial \hat{u}_{m,n}}{\partial \hat{x}} - \mathcal{B}_v \eta \frac{\partial \hat{u}_{m,n}}{\partial \eta} + \frac{\partial \hat{v}_{m,n}}{\partial \eta} + in\hat{w}_{m,n} = 0; \tag{2.19}$$

b. the x-momentum equation

$$[s^2(-im\hat{k}_1 + n^2 k_3^2) + 2\mathcal{B}_v U_B + s^2 U_{B\hat{x}} - \mathcal{B}_v \eta U_{B\eta} + s^2 ink_3 W_B]\hat{u}_{m,n} + s^2 U_B \frac{\partial \hat{u}_{m,n}}{\partial \hat{x}}$$

$$+ (sV_B - \mathcal{B}_v \eta U_B)\frac{\partial \hat{u}_{m,n}}{\partial \eta} - \frac{\partial^2 \hat{u}_{m,n}}{\partial \eta^2} + U_{B\eta}\hat{v}_{m,n} = -r_t s^2 \hat{l}_{m,n}; \tag{2.20}$$

c. the y-momentum equation

$$[s^2(-im\hat{k}_1 + n^2 k_3^2) + \mathcal{B}_v U_B + sV_{B\eta} + s^2 ink_3 W_B]\hat{v}_{m,n}$$

$$+ (s^3 V_{B\hat{x}} - s\mathcal{B}_v \eta V_{B\eta} + 2s^3 G_\Lambda \chi_B U_B)\hat{u}_{m,n} + s^2 U_B \frac{\partial \hat{v}_{m,n}}{\partial \hat{x}}$$

$$+ (sV_B - \mathcal{B}_v \eta U_B)\frac{\partial \hat{v}_{m,n}}{\partial \eta} - \frac{\partial^2 \hat{v}_{m,n}}{\partial \eta^2} + \frac{\partial \hat{p}_{m,n}}{\partial \eta} = -r_t s^2 \hat{e}_{m,n}; \tag{2.21}$$

920 A14-11

d. the z-momentum equation

$$
s^2(-im\hat{k}_1 + n^2k_3^2 + ink_3W_B)\hat{w}_{m,n} + s^2U_B\frac{\partial\hat{w}_{m,n}}{\partial\hat{x}} + (sV_B - \mathcal{B}_v\eta U_B)\frac{\partial\hat{w}_{m,n}}{\partial\eta}
$$

$$
- \frac{\partial^2\hat{w}_{m,n}}{\partial\eta^2} + (W_{B\hat{x}}s^2 - \mathcal{B}_v\eta W_{B\eta})k_3s^2\hat{u}
$$

$$
+ s^2k_3W_{B\eta}\hat{v} + s^2(ink_3^2)\hat{p}_{m,n} = -r_ts^2\hat{h}_{m,n}, \tag{2.22}
$$

where $\mathcal{B}_v = (U_e - \hat{x}U'_e)/U_e^2$ with a prime denoting differentiation with respect to $\hat{x}$. The expressions for the nonlinear terms, $\hat{l}_{m,n}$, $\hat{e}_{m,n}$ and $\hat{h}_{m,n}$, are given in Xu (2020). Equations (2.19)–(2.22) are different from (2.47)–(2.50) in Xu *et al.* (2020) due to the extra terms involving W_B as well as to the fact that U_B and V_B are part of the solution to be found instead of being the unperturbed base flow.

Before solving the NUBRE system, some remarks on its nature and relation to the NPSE (nonlinear parabolised stability equations) (Herbert 1997) are in order. The latter were derived for a perturbation to a given spatially varying base flow, and a key step to characterising the fast spatial variation of the perturbation by defining a finite local streamwise wavenumber, which is usually done by an *ad hoc* approximation. NUBRE exhibit several key differences from the NPSE despite apparent similarity. First of all, the most general NUBRE (2.9) are an appropriate asymptotic reduction of the N–S equations. When the flow field is decomposed into a given base flow and a small-amplitude perturbation about it, the resulting equations are akin to the NPSE, and indeed can be considered as the special form of NPSE with the local streamwise wavenumber being zero, and a natural one too in the sense that the zero streamwise wavenumber follows from the asymptotic scaling rather than an *ad hoc* procedure. Historically, NUBRE had been established (Hall 1988) before NPSE approach was. Secondly, NUBRE can describe the evolution of perturbations that have a magnitude as large as the base flow and hence are strongly nonlinear. Indeed, as is the case here, there is no need to prescribe an unperturbed base flow. In contrast, NPSE are applicable only to weakly nonlinear small-amplitude perturbations. Thirdly, NPSE can describe rather general forms of perturbations provided that their streamwise length scales are long. As such they can be employed to study the response (receptivity) to various forms of long-wavelength external disturbances such as wall roughness and FSVD. NPSE are restricted to perturbations of a local modal form, and cannot describe the receptivity to external disturbances. The required initial condition for downstream marching must be provided by a separate means.

The system of coupled equations, (2.13*a–c*) and (2.14) or equivalently (2.19)-(2.22), is to be solved subject to appropriate far-field (boundary) and upstream (initial) conditions, which we shall present next.

2.2. *Far-field condition: disturbances at the outer edge of the boundary layer*

In the outer region IV, the disturbance is governed by the large-y limit of the NUBRE (2.14). On noting that $\hat{u}$ and W_B both tend to be zero in the limit $y \to \infty$, the centrifugal force and $V_{B\hat{x}}\hat{u}$ terms drop out of the wall-normal momentum equation in (2.14), which reduces to

$$
\left.\begin{array}{r}
\hat{v}_{\hat{\tau}} + U_e\hat{v}_{\hat{x}} + V_e\hat{v}_y + \hat{v}V_{ey} + \hat{v}\hat{v}_y + \hat{w}\hat{v}_z = -\hat{p}_y + \hat{v}_{yy} + \hat{v}_{zz}, \\
\hat{w}_{\hat{\tau}} + U_e\hat{w}_{\hat{x}} + V_e\hat{w}_y + \hat{v}\hat{w}_y + \hat{w}\hat{w}_z = -\hat{p}_z + \hat{w}_{yy} + \hat{w}_{zz}, \\
\hat{v}_y + w_z = 0,
\end{array}\right\} \tag{2.23}
$$

where $V_e(\hat{x}, y)$ characterises the behaviour of the wall-normal velocity at the outer edge of region III. By integrating the continuity equation in (2.13a–c) with respect to y from 0 to ∞, we obtain

$$V_e \to -U'_e(\hat{x})y + \bar{v}_0 \quad \text{as } y \to \infty, \tag{2.24}$$

where $\bar{v}_0 = (sU_e\bar{\delta})_{\hat{x}}$ with $\bar{\delta}$ being the boundary-layer thickness $\bar{\delta}$, defined as

$$\bar{\delta} = \frac{k_3}{2\pi} \int_0^{2\pi/k_3} \int_0^\infty \left(1 - \frac{U_B}{U_e}\right) d\eta \, dz. \tag{2.25}$$

It transpires that $\bar{v}_0$ represents the transpiration velocity induced by the displacement effect of the viscous motion in region III. The coupling of $\hat{v}$ and $\hat{w}$ with $\bar{v}_0$ in (2.23) can be removed by the generalised Prandtl transformation (Xu *et al.* 2020),

$$\hat{y} = U_e y - \hat{\delta}(\hat{x}, \hat{\tau}), \tag{2.26}$$

where $\hat{\delta}$ is chosen to remove the dependence on $\bar{v}_0$, and this requires that $\hat{\delta}$ satisfies the equation,

$$\hat{\delta}_{\hat{\tau}} + U_e\hat{\delta}_{\hat{x}}(\hat{x}, \hat{\tau}) = U_e(sU_e\bar{\delta})_{\hat{x}}. \tag{2.27}$$

The appropriate 'boundary condition' is

$$\hat{\delta}(0, \hat{\tau}) = 0 \quad \text{for all } \hat{\tau} > 0, \tag{2.28}$$

which corresponds to a vanishingly small displacement near the leading edge. It is noted that for steady FSVD, the linear inhomogeneous equation (2.27) has the solution,

$$\hat{\delta} = sU_e\bar{\delta}. \tag{2.29}$$

Equation (2.23) for $\hat{v}$ and $\hat{w}$ were rewritten in terms of $\hat{y}$ and solved by Xu *et al.* (2020). Using the solution and the matching principle, the far-field condition is constructed as

$$(\hat{u}_{m,n}, \hat{v}_{m,n}, \hat{w}_{m,n}, \hat{p}_{m,n}) \to (0, s^{-1}\hat{v}^\dagger_{m,n}, k_3\hat{w}^\dagger_{m,n}, \epsilon R_\Lambda \hat{p}^\dagger_{m,n}) \quad \text{as } \eta \to \infty, \tag{2.30}$$

where

$$\left.\begin{array}{l}
\hat{v}^\dagger_{m,\pm 1} = k_3/U_e \hat{c}_\infty \mathcal{A}_v[e^{i(\varphi_1+k_2U_ey)}\phi_m + e^{-i(\varphi_1+k_2U_ey)}\phi^*_{-m}], \\[4pt]
\hat{w}^\dagger_{m,\pm 1} = \mp k_2 \hat{c}_\infty \mathcal{A}_v[e^{i(\varphi_1+k_2U_ey)}\phi_m - e^{-i(\varphi_1+k_2U_ey)}\phi^*_{-m}], \\[4pt]
\hat{p}^\dagger_{m,\pm 1} = \frac{1}{r_t}\hat{p}_\infty \mathcal{A}_v[e^{i(\varphi_1+k_2U_ey)}\phi_m + e^{-i(\varphi_1+k_2U_ey)}\phi^*_{-m}], \\[4pt]
\hat{p}^\dagger_{m,0} = -2(k_3^2/U_e^2)\hat{c}_\infty^2\mathcal{A}_v^2[e^{2i(\varphi_1+k_2U_ey)}\pi_m + e^{-2i(\varphi_1+k_2U_ey)}\pi^*_{-m}], \\[4pt]
\hat{p}^\dagger_{0,\pm 2} = 2k_2^2\hat{c}_\infty^2\mathcal{A}_v^2.
\end{array}\right\} \tag{2.31}$$

Here, ϕ_m and π_m are computed according to the Fourier transforms,

$$(e^{i\hat{k}_1\hat{\tau}-ik_2\hat{\delta}(\hat{x},\hat{\tau})}, e^{2i\hat{k}_1\hat{\tau}-2ik_2\hat{\delta}(\hat{x},\hat{\tau})}) = \sum_m (\phi_m(\hat{x}), \pi_m(\hat{x})) \, e^{-im\hat{k}_1\hat{\tau}}. \tag{2.32}$$

The notations in (2.31) are defined as

$$\left.\begin{array}{l}
\hat{c}_\infty = -\hat{u}_3^\infty (U_e^2/\chi^2)(k_2^2 + k_3^2)/k_2, \quad \hat{p}_\infty = 2ik_3(U_e^2/\chi^2)U'_e(k_2^2 + k_3^2)\hat{u}_3^\infty, \\[8pt]
\varphi_1 = \hat{k}_1 \int_0^{\hat{x}} (1/U_e) \, d\hat{x}, \quad \mathcal{A}_v = \exp\left\{-\int_0^{\hat{x}} \frac{1}{U_e}(U_e^2 k_2^2 + k_3^2) \, d\hat{x}\right\}, \\[8pt]
\chi = [(k_1/U_e)^2 + (k_2 U_e)^2 + k_3^2]^{1/2}.
\end{array}\right\} \tag{2.33}$$

All other components $\hat{v}^\dagger_{m,n} = \hat{w}^\dagger_{m,n} = 0$ $(n \neq \pm 1)$, and $\hat{p}^\dagger_{m,n} = 0$ $(n \neq 0, \pm 1, \pm 2)$. Note that the entrainment process is interactive with the mutual influence between the streaky

boundary layer and the FSVD in the outer region IV being facilitated through (2.25), (2.27) and (2.30) with (2.32).

2.3. *Initial condition*

In the upstream limit $\hat{x} \to 0$, the solution of the NUBRE (2.19)-(2.22) can be constructed in the form of power series of s, and the solution in the region covering $y = O(1)$ up to $1 \ll y < R_\Lambda$, was constructed in Xu *et al.* (2020). Using these solutions, the composite initial condition for the spanwise-varying components can be expressed as

$$\hat{u}_{1,\pm 1} \to q_\pm (2\hat{x}/s^2)(U_0 + sU_1), \tag{2.34}$$

$$\hat{v}_{1,\pm 1} \to q_\pm \left\{ V_0 + sV_1 + \frac{\mathrm{i}\mathcal{A}_v \exp\{\mathrm{i}(\varphi_1 - U_e k_2 s\beta)\}}{(U_e k_2 - \mathrm{i}|k_3|)s} (\mathrm{e}^{\mathrm{i}U_e k_2 s\eta} - \mathrm{e}^{-|k_3|s\eta}) \right.$$
$$\left. + \mathrm{e}^{-|k_3|s\eta} \left(\frac{\beta}{4} + sc_1 \right) - \bar{v}_c \right\}, \tag{2.35}$$

$$\hat{w}_{1,\pm 1} \to \mp \mathrm{i}q_\pm \left\{ W_0 + sW_1 + \frac{U_e k_2 \mathcal{A}_v \exp\{\mathrm{i}(\varphi_1 - U_e k_2 s\beta)\}}{(U_e k_2 - \mathrm{i}|k_3|)} (\mathrm{e}^{\mathrm{i}U_e k_2 s\eta} - \mathrm{e}^{-|k_3|s\eta}) \right.$$
$$\left. + \mathrm{e}^{-|k_3|s\eta} \left[1 - \beta \left(\mathrm{i}U_e k_2 - \frac{|k_3|}{4} \right) s \right] - \bar{w}_c \right\}, \tag{2.36}$$

as $\hat{x} \to 0$, where

$$q_\pm = \pm \mathrm{i}|k_3|(k_2^2 + k_3^2)(U_e \hat{u}_{3,\pm}^\infty \pm \mathrm{i}\hat{u}_{2,\pm}^\infty)U_e/\chi^2 = (\pm \mathrm{i}|k_3|/k_2)(k_2^2 + k_3^2)(k_2 U_e - \mathrm{i}|k_3|),$$

$$\bar{v}_c = -\eta + \frac{\beta}{4} + s \left[-\frac{\mathrm{i}}{2}(U_e k_2 + \mathrm{i}|k_3|)\eta^2 + \beta \left(\mathrm{i}U_e k_2 - \frac{|k_3|}{4} \right) \eta + c_1 \right], \tag{2.37}$$

$$\bar{w}_c = 1 + s \left[\mathrm{i}(U_e k_2 + \mathrm{i}|k_3|)\eta - \beta \left(\mathrm{i}U_e k_2 - \frac{|k_3|}{4} \right) \right]. \tag{2.38}$$

The constant c_1 is obtained numerically along with U_k, V_k and W_k ($k = 0, 1$) by solving (B1)–(B8) of Leib *et al.* (1999) provided that the κ^2 in (B7) is replaced by k_3^2.

3. Numerical methods

The coupled system, (2.13*a–c*) and (2.19)–(2.22), the far-field condition (2.30) with (2.31) and the initial condition (2.34)–(2.36) all together form the initial-boundary-value problem that describes the development of the streaky boundary layer under the influence of FSVD. It is solved numerically using the methods described in this section.

3.1. *Steady spanwise-averaged velocities*

The boundary-layer equations (2.13*a–c*) governing the spanwise-averaged velocities, U_B and V_B, can be rewritten in terms of $\hat{x}$ and η as

$$\left. \begin{aligned} \frac{\partial U_B}{\partial \hat{x}} - \frac{\eta B_v}{s^2}\frac{\partial U_B}{\partial \eta} + \frac{1}{s}\frac{\partial V_B}{\partial \eta} &= 0, \\ U_B \left(\frac{\partial U_B}{\partial \hat{x}} - \frac{\eta B_v}{s^2}\frac{\partial \hat{U}_B}{\partial \eta} \right) + \frac{V_B}{s}\frac{\partial U_B}{\partial \eta} &= -\frac{\mathrm{d}P_B}{\mathrm{d}\hat{x}} + \frac{1}{s^2}\frac{\partial^2 U_B}{\partial \eta^2} + Q_1. \end{aligned} \right\} \tag{3.1}$$

Introduce the streamfunction Ψ_B such that $U_B = \Psi_{B,y}$ and $V_B = -\Psi_{B,\hat{x}}$. Let

$$\Psi_B = U_e s F(\hat{x}, \eta), \tag{3.2}$$

where $F(\hat{x}, \eta)$ is introduced for simplification. It follows that

$$\left.\begin{aligned} U_B &= \Psi_{B,y} = U_e \frac{\partial F}{\partial \eta}, \\ V_B &= -\Psi_{B,\hat{x}} = -\left(\frac{dU_e}{d\hat{x}} s F + U_e \frac{ds}{d\hat{x}} F + U_e s \frac{\partial F}{\partial \hat{x}} - \frac{U_e \eta}{s} B_v \frac{\partial F}{\partial \eta} \right). \end{aligned}\right\} \tag{3.3}$$

Substituting (3.3) into (3.1), we obtain the equation for F,

$$F''' + \frac{m+2}{2} F F'' + m(1 - F'^2) = 2\hat{x} \left(F' \frac{\partial F'}{\partial \hat{x}} - \frac{\partial F}{\partial \hat{x}} F'' - \frac{Q_1}{U_e^2} \right), \tag{3.4}$$

where $m = s^2 U_e'$ and a prime on F denotes the differentiation with respect to η. In the upstream limit $\hat{x} \to 0$, F satisfies the Blasius equation,

$$F''' + F F'' = 0, \tag{3.5}$$

and the boundary conditions are

$$F' = F = 0 \quad \text{at } \eta = 0, \quad F' = U_e(\hat{x}) \quad \text{as } \eta \to \infty. \tag{3.6a,b}$$

For convenience of numerical integration, we recast (3.4) into a system of first-order equations by introducing new variables $U(\hat{x}, \eta)$ and $G(\hat{x}, \eta)$,

$$U = F', \quad G = U'. \tag{3.7a,b}$$

The ordinary differential equations (3.7a,b) are discretised using the finite-difference scheme centred at the midpoint $(\hat{x}^n, \eta_{j-1/2})$,

$$\frac{U_j^n + U_{j-1}^n}{2} = \frac{F_j^n - F_{j-1}^n}{\Delta \eta_j} = U_{j-1/2}^n, \quad \frac{G_j^n + G_{j-1}^n}{2} = \frac{U_j^n - U_{j-1}^n}{\Delta \eta_j} = G_{j-1/2}^n, \tag{3.8a,b}$$

where $(\hat{x}^n, \eta_j)$ stands for a mesh point. Similarly, the partial differential equation (3.4) is approximated by a finite difference centred at the midpoint $(\hat{x}^{n-1/2}, \eta_{j-1/2})$, which is done in two steps. In the first, we discretise (3.4) in the streamwise direction at $(\hat{x}^{n-1/2}, \eta)$ without specifying η (Cebeci & Cousteix 2005), and the resulting equation is discretised with respect to η centred at $(\hat{x}^{n-1/2}, \eta_{j-1/2})$ to obtain

$$\Delta \eta_j^{-1} (G_j^n - G_{j-1}^n) + \alpha_1 (FG)_{j-1/2}^n - \alpha_2 (U^2)_{j-1/2}^n$$

$$+ \alpha^n (G_{j-1/2}^{n-1} F_{j-1/2}^n - F_{j-1/2}^{n-1} G_{j-1/2}^n) = R_{j-1/2}^{n-1} - 4\hat{x}^{n-1/2} \frac{Q_{1,j-1/2}^{n-1/2}}{(U_e^2)_{j-1/2}^{n-1/2}}, \tag{3.9}$$

where

$$\alpha^n = \frac{2\hat{x}^{n-1/2}}{\Delta \hat{x}}, \quad \alpha_1 = \frac{m^n + 2}{2} + \alpha^n, \quad \alpha_2 = m^n + \alpha^n, \tag{3.10a–c}$$

$$R_{j-1/2}^{n-1} = -L_{j-1/2}^{n-1} + \alpha^n [(FG)_{j-1/2}^{n-1} - (U^2)_{j-1/2}^{n-1}] - m^n, \tag{3.11}$$

$$L_{j-1/2}^{n-1} = \left[\Delta \eta_j^{-1} (G_j - G_{j-1}) + \frac{m+2}{2} (FG)_{j-1/2} + m[1 - (U^2)_{j-1/2}] \right]^{n-1}, \tag{3.12}$$

for $j = 1, 2, \ldots, J - 1$ with J being the number of mesh points in the wall-normal direction. The boundary conditions (3.6a,b) at $\hat{x} = \hat{x}^n$ give

$$F_0^n = U_0^n = 0, \quad U_J^n = 1. \tag{3.13a,b}$$

The system of nonlinear algebraic equations, (3.8a,b) and (3.9), is solved by using Newton's iteration, the detail of which is relegated to Appendix A.

After Newton's iteration yields the convergent solution for U_B and V_B, we seek the solution for W_B, the equation for which in (2.13a–c) can be recast into a first-order system,

$$\left.\begin{array}{c} W_{B\eta} = H, \\ U_B \left(\dfrac{\partial W_B}{\partial \hat{x}} - \dfrac{\eta B_v}{s^2} H \right) + \dfrac{V_B}{s} H = \dfrac{1}{s^2} H_\eta + Q_3. \end{array}\right\} \tag{3.14}$$

Discretisation of (3.14) at $(\hat{x}^{n-1/2}, \eta_{j-1/2})$ gives the difference equations,

$$\left.\begin{array}{c} (W_j^n - W_{j-1}^n) - \dfrac{\Delta \eta_j}{2}(H_j^n + H_{j-1}^n) = 0, \\ S_1 W_{Bj}^n + S_1 W_{Bj-1}^n + \frac{1}{2}(S_2^- H_j^n + S_2^+ H_{j-1}^n) \\ = S_1 W_{Bj}^{n-1} + S_1 W_{Bj-1}^{n-1} - \frac{1}{2}(S_2^- H_j^{n-1} + S_2^+ H_{j-1}^{n-1}) + (Q_3)_{j-1/2}^{n-1/2}, \end{array}\right\} \tag{3.15}$$

where

$$S_1 = \frac{1}{2\Delta \hat{x}} U_{Bj-1/2}^{n-1/2}, \quad S_2^\pm = -\left(\frac{\eta B_v}{2s^2} U_B\right)_{j-1/2}^{n-1/2} + \left(\frac{V_B}{2s}\right)_{j-1/2}^{n-1/2} \pm \frac{1}{s_{n-1/2}^2 \Delta \eta_j}. \tag{3.16a,b}$$

The initial and boundary conditions are

$$W_j^0 = 0 \quad (j = 0, 1, \ldots, J), \quad W_0^n = W_J^n = 0. \tag{3.17a,b}$$

The solution to (3.15) is obtained again by using the block elimination method.

3.2. *Unsteady or spanwise-varying velocities and pressure*

We define the solution vector $U = (\hat{u}, \hat{v}, \hat{w}, \hat{u}_\eta, \hat{p}, \hat{w}_\eta)$ and recast (2.19)–(2.22) into a system of first-order equations,

$$\frac{\partial U}{\partial \eta} = C_0 U + C_1 \frac{\partial U}{\partial \hat{x}} + f(U), \tag{3.18}$$

where the subscripts 'm, n' are omitted for brevity, $f(U)$ stands for nonlinear terms and the constitute elements of the coefficient matrices C_0 and C_1 are given in Appendix B.

For unsteady spanwise uniform components with $n = 0$ but $m \neq 0$, $\hat{u}$ and $\hat{v}$ are decoupled from $\hat{w}$, and the system (2.19)–(2.22) can be simplified to three equations for $\hat{u}$,

920 A14-16

$\hat{v}$ and $\hat{f} \equiv \hat{u}_\eta$:

$$\left.\begin{aligned}
\hat{u}_\eta &= \hat{f}, \quad \hat{v}_\eta = -2\mathcal{B}_v\hat{u} + \mathcal{B}_v\eta\hat{f} - s^2\hat{u}_{\hat{x}}, \\
\hat{f}_\eta &= [s^2(-im\hat{k}_1) + 2\mathcal{B}_v U_B + s^2 U_{B\hat{x}} - \mathcal{B}_v\eta U_{B\eta}]\hat{u} \\
&\quad + U_{B\eta}\hat{v} + (-\mathcal{B}_v\eta U_B + sV_B)\hat{f} + s^2 U_B\hat{u}_{\hat{x}} + r_t s^2\hat{l}_{m,0};
\end{aligned}\right\}
\tag{3.19}$$

and two equations for $\hat{w}$ and $\hat{g} \equiv \hat{w}_\eta$,

$$\left.\begin{aligned}
\hat{w}_\eta &= \hat{g}, \\
\hat{g}_\eta &= (W_{B\hat{x}}s^2 - \mathcal{B}_v\eta W_{B\eta})k_3 s^2\hat{u} + W_{B\eta}k_3 s^2\hat{v} + s^2(-im\hat{k}_1)\hat{w} \\
&\quad + (-\mathcal{B}_v\eta U_B + sV_B)\hat{g} + s^2 U_B\hat{w}_{\hat{x}} + r_t s^2\hat{h}_{m,0}.
\end{aligned}\right\}
\tag{3.20}$$

The streamwise parabolic NUBRE (3.18) can be solved by a marching procedure in $\hat{x}$-direction. As in Xu *et al.* (2017, 2020), the two-point compact scheme of Malik (1990) and the second-order backward finite-difference scheme are applied in the η and streamwise directions, respectively. Grouping all the terms at the streamwise location $n+1$ on the left-hand side (except the nonlinear terms), we end up with the discrete equations,

$$\left[I - \frac{h}{2}c_{j+1}\right]U_{j+1}^{n+1} + \left[-I - \frac{h}{2}c_j\right]U_j^{n+1} = \frac{h}{2}[g_{j+1} + g_j] + \frac{h}{2}[f(U_{j+1}^{n+1}) + f(U_j^{n+1})],
\tag{3.21}$$

where I is the unit matrix, and we have put

$$f(U_j^{n+1}) = (0 \quad 0 \quad 0 \quad -\hat{l}, \quad -\mathcal{B}_v\eta\hat{l} + \hat{e}, \quad -\hat{h})_j^{n+1},
\tag{3.22}$$

$$c_{j+1} = C_{0,j+1} + \frac{3}{2\Delta\hat{x}}C_{1,j+1}, \quad g_{j+1} = C_{1,j+1}\left(-2U_{j+1}^n + \frac{1}{2}U_{j+1}^{n-1}\right)/\Delta\hat{x}.
\tag{3.23a,b}$$

On introducing the discrete solution vector,

$$\Phi_{n+1} = (U_J^{n+1}, \quad U_{J-1}^{n+1}, \quad \cdots, \quad U_1^{n+1}, \quad U_0^{n+1})^{\mathrm{T}},
\tag{3.24}$$

the system of nonlinear algebraic equations, (3.21), is written in the matrix form,

$$L\Phi_{n+1} = A + N_{n+1},
\tag{3.25}$$

where L is the 'linear' operator, A stands for the terms whose values are evaluated at upstream positions and N_{n+1} denotes the nonlinear terms. Discretisation of (3.19) and (3.20) leads to algebraic systems similar to (3.25). The so-called 3/2-rule is followed in order to eliminate the aliasing error (Kim, Moin & Moser 1987). Seventeen Fourier modes are retained for capturing nonlinear effects, but more Fourier modes are needed for strong adverse-pressure-gradient cases. In the present study, 33 Fourier modes proved to be sufficient. The domain size in the $\eta-$direction is 30, within which 1000 grid points are deployed. The computation domain starts from $\hat{x} = 0.001$. In most calculations, we take the streamwise marching step $\Delta\hat{x} = 0.001$, but stronger adverse-pressure-gradient case requires a smaller $\Delta\hat{x}$.

In order to obtain the convergent solution of the NUBRE, an underrelaxtion predictor–corrector procedure is applied. The marching from location n to $n+1$ involves the three steps as follows.
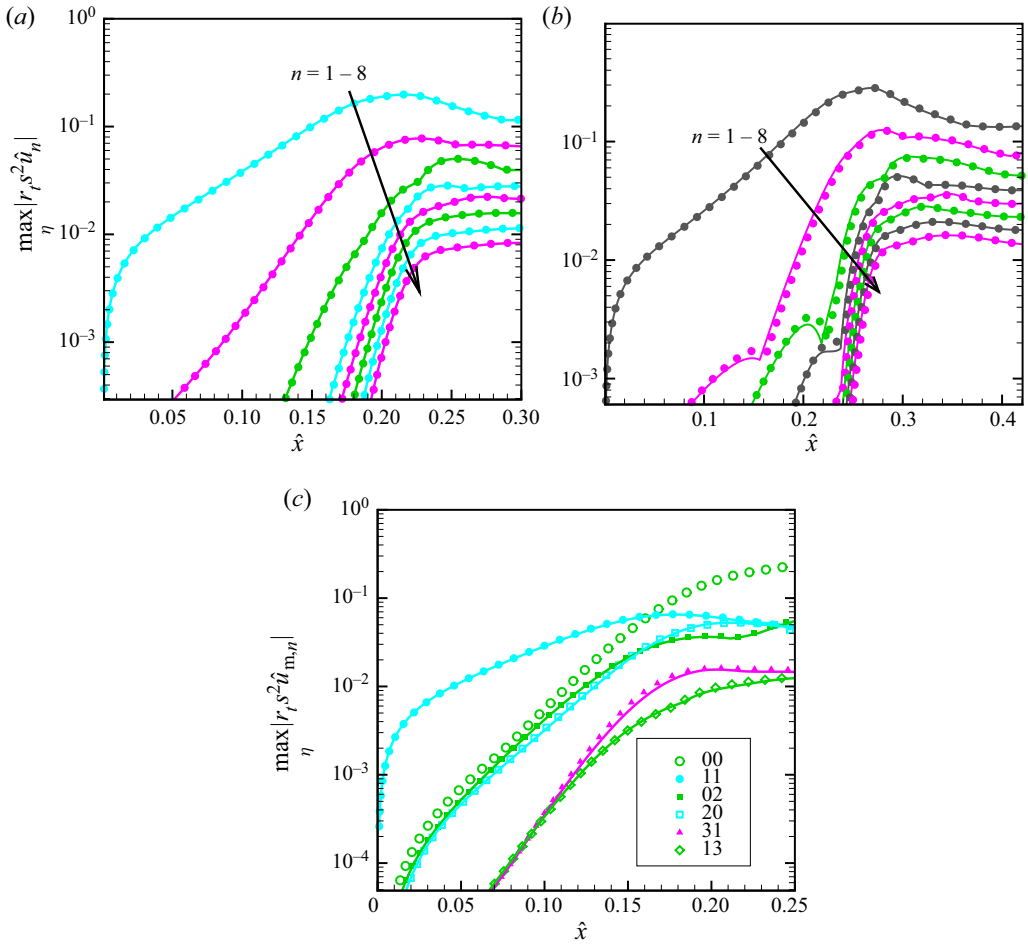
Figure 2. Validation of the numerical algorithm and code. The downstream development of the maximum streamwise velocity of different Fourier modes. (*a*) Zero-pressure-gradient case $\sigma_c = 0$, (*b*) a favourable gradient case $\sigma_c = 1.5$ and (*c*) an unsteady adverse gradient case $\sigma_c = 0.8$. The parameters are $\hat{k}_1 = 26.35$, $G_\Lambda = 1501$, $R_\Lambda = 1145$ and $\epsilon = 0.0007$. The solid lines indicate the results obtained by the present algorithm, whereas the symbols stand for the results of Xu *et al.* (2017) (*a*) and Xu (2020) (*b*,*c*).

Step 1: the nonlinear terms and the steady spanwise-averaged velocities in (3.25) and the related systems for (3.19) and (3.20) are approximated by using the values of the variables at the streamwise location *n*.

Step 2: systems (3.25), (3.19) and (3.20) are marched forward to predict the spanwise-dependent and unsteady spanwise uniform components at the location $n + 1$. These are updated by an underrelaxation iteration (Xu *et al.* 2017, 2020) with the spanwise-averaged velocities being fixed at the value the streamwise location *n*. The iteration continues until convergence is achieved.

Step 3: update the forcing terms Q_1 and Q_3 using the output for the unsteady and spanwise-dependent components from step 2. Compute the steady spanwise-averaged velocities, namely solve (3.8*a*,*b*) and (3.9) for U_B and V_B at $(n + 1)$, and solve (3.15) for W_B at $(n + 1)$.

920 A14-18
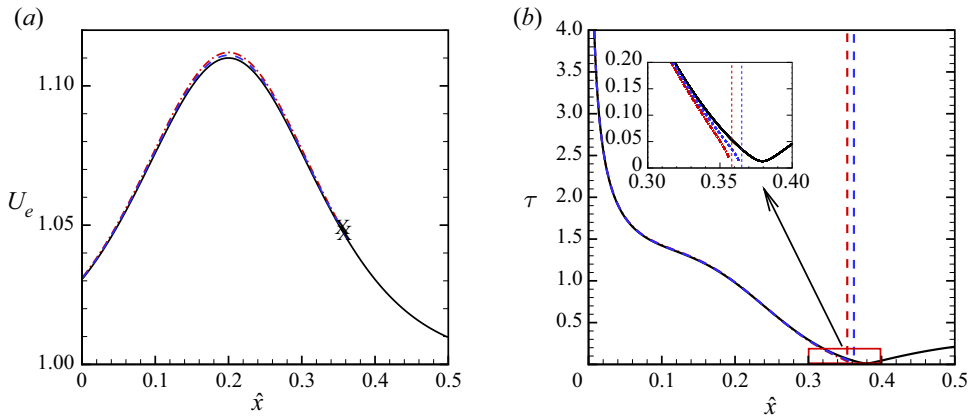
Figure 3. The slip velocity (*a*) and the skin friction (*b*) for a favourable-to-adverse flow. The dash-dotted and dashed lines represent the results for $d = 0.112$ and 0.111, respectively. The solid lines are the results at $d = 0.110$, which are included for comparison. The vertical dashed lines mark the approximate location where $\tau = 0$. The inset displays an enlarged view of the part in the box.

Repeat steps 2 and 3 until both the steady spanwise-averaged and unsteady or spanwise-dependent quantities converge.

For the purpose of validation, the present algorithm and code are applied to several cases, which were investigated previously using a different algorithm and code. The comparison is shown in figure 2, and the agreement is clearly very good.

4. Numerical results

4.1. *Flat-plate case: streaks eliminate separation*

The flow over an aerofoil is often subject to a favourable-to-adverse pressure gradient (Istvan *et al.* 2017; Istvan & Yarusevych 2018). Such a form of pressure gradient is also imposed to the flat-plate model in experiments (e.g. Gaster 1966; Michelis *et al.* 2018), which can mimic the conditions on the suction side of a highly cambered airfoil of finite thickness. In the present paper, the induced slip velocity is assumed to be

$$U_e(\hat{x}) = 1 + d\{\tanh^2[(\hat{x} - \hat{x}_0)\pi/L] - 1\}, \tag{4.1}$$

where $\hat{x}_0$ is the location where the slip velocity attains its maximum, the parameters d and L control the intensity and the streamwise extent of the pressure gradient, respectively. We choose $\hat{x}_0 = 0.2$ and $L = 0.5$ in the present work. Figure 3(*a*) shows the distribution of $U_e(\hat{x})$ for several values of d.

The discretised boundary-layer equations (3.8*a,b*) and (3.9) are first solved in the absence of FSVD. A convergent solution can be obtained for all $\hat{x}$ for $d \leq 0.110$. However, marching cannot continue beyond a certain streamwise location for $d = 0.111$, indicating that the critical value for the onset of separation is $d_c \approx 0.111$. The slip velocity with $d = 0.111$ or 0.112 is expected to induce a two-dimensional short separation bubble. Figure 3(*b*) displays the evolution of the skin friction $\tau = \partial u/\partial y$. Since the classical boundary-layer theory cannot describe such a flow, convergent solutions cannot be obtained at or beyond the marked location $\hat{x}_s$ where $\tau = 0$. The enlarged view in the inserted window shows that as $d \to d_c$, the skin friction approaches the asymptotic behaviour $\tau \sim |\hat{x}_s - \hat{x}|$ (Ruban 1981). It is also shown that with the increase of the adverse-pressure-gradient intensity d, the separation location moves forward.
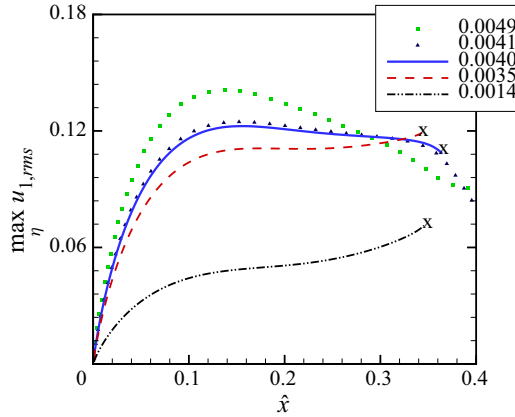
Figure 4. Comparison of the downstream development of $\max_\eta u_{1,rms}$ for steady FSVD with different ϵ. The symbols **x** indicate the separation locations. The parameters are $d = 0.112$, $G_\Lambda = 0$ and $R_\Lambda = 1145$.

In all the calculations, the parameters characterising FSVD are specified as follows. We take spanwise wavenumber $k_3 = 1$ without losing generality, and $k_2 = k_3$ is chosen on the consideration that FSVD are typically 'axisymmetric'. Since $k_1 = 0$ or $k_1 \ll 1$ (steady or low-frequency FSVD), it follows from (2.5) that $\hat{u}_{2,\pm}^\infty = \mp\hat{u}_{3,\pm}^\infty$; we take $\hat{u}_{3,+}^\infty = -\hat{u}_{3,-}^\infty = 1$ since the oblique components in the pair are assumed to have an equal amplitude and $\hat{u}_{3,+}^\infty$ can be absorbed into ϵ.

In this section, our results will confirm that three-dimensional disturbances induced by low-frequency FSVD of rather moderate intensity can eliminate the two-dimensional separation. The intensity of the vortices generated is to be measured by $u_{1,rms}$, the root-mean-square of the spanwise-dependent harmonic components, which is defined as

$$u_{1,rms} \equiv r_t \left[\sum_{m,n \neq 0} |s^2 \hat{u}_{m,n}|^2 \right]^{1/2}. \tag{4.2}$$

It should be noted that in the steady limit $\hat{k}_1 = 0$, the double summation in (4.2) reduces to a single sum. The development of $u_{1,rms}$ is shown in figure 4 for five different values of ϵ. In the linear stage, $u_{1,rms}$ amplifies rapidly and the amplification becomes moderate in the nonlinear saturating stage, which commences in the region of favourable pressure gradient (acceleration). The amplitude attained increases with ϵ. For $\epsilon < 0.35$, $u_{1,rms}$ amplifies again past $\hat{x} \approx 0.2$, the start of the decelerating (adverse-pressure-gradient) region. This is because, under an adverse pressure gradient, the disturbance starts to saturate only after it has reached an amplitude larger than that under favourable pressure gradient (see figure 3 in Xu *et al.* 2020). Presently, the amplitude at $\hat{x} \approx 0.2$ is below that required for saturation. For $\epsilon \geq 0.4$, the amplitude acquired in the accelerating region is already large enough for nonlinearity to inhibit the growth in the decelerating region $\hat{x} > 0.2$ and so saturation continues. For $\epsilon \leq 0.0040$, our code to solve the NUBRE 'blows up', signifying that the solution then terminates at a finite-distance singularity. However, in the presence of FSVD with higher intensity levels $\epsilon = 0.0041$ and 0.0049, separation does not occur any longer. The present result indicates that the threshold amplitude ϵ_c for FSVD to eliminate the separation is $0.0040 < \epsilon_c < 0.0041$. For $\epsilon = 0.0041$, which is only slightly above ϵ_c, the extended saturation is followed by rather rapid attenuation. For a sufficiently high ϵ
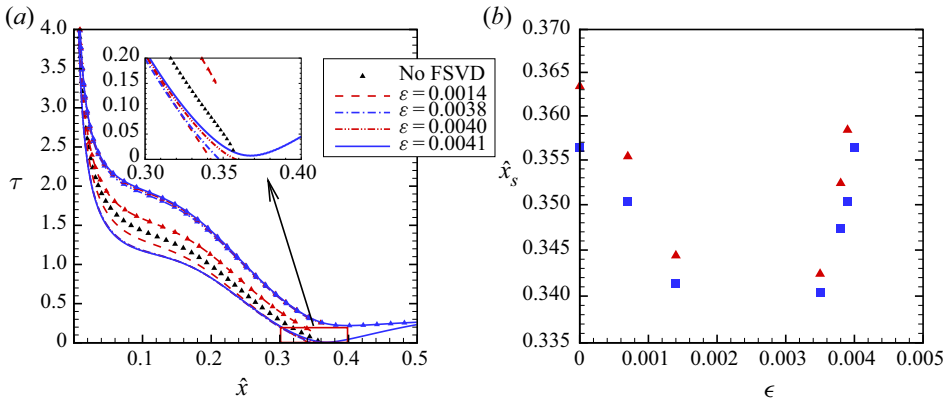
920 A14-20

Figure 5. (*a*) The development of the skin frictions at the valley and peak for $d = 0.112$ and different FSVD level ϵ. The symbols present the skin frictions at the peak. (*b*) The streamwise location of the separation vs ϵ. The squares and deltas refer to the cases of $d = 0.112$ and 0.111, respectively.

(0.0049), $u_{1,rms}$ features a broad peak rather than extended saturation and then decays rather gradually.

The reader is reminded that in the present study, the FSVD intensity ϵ is gradually increased in order to identify the critical level ϵ_c. Our theory is completely appropriate when $\epsilon > \epsilon_c$ because in the absence of separation, the viscous effect produces merely an asymptotically small correction to the inviscid main flow, and specifically the two-dimensional pressure gradient induced by the viscous motion is negligible in comparison with the streamwise inertia in the boundary layer, while the displacement effect on FSVD, which appears at leading order, has already been taken into account in our analysis and computations. However, the solutions for $\epsilon < \epsilon_c$ must be treated with caution because the massively separated flow may influence the entire inviscid part of the main flow. An appropriate description of a separated boundary layer in the case of $\epsilon < \epsilon_c$ is beyond the scope of the present paper and requires a new approach.

Figure 5(*a*) displays the downstream development of the skin frictions at the peak and valley. The result indicates that our code to solve the NUBRE 'blows up' where the minimum skin friction approaches zero, suggesting that the termination is associated with separation. The separation location depends on the FSVD level. In the case of $d = 0.112$ and $\epsilon \geq 0.0040$, τ reaches its minimum which is positive and then increases, and marching can be continued to arbitrary locations downstream, suggesting that the FSVD at the present level has suppressed the separation completely. Specifically at $\epsilon = 0.0041$, the skin friction undergoes a sharply decrease at the very beginning. Then the skin frictions at the peak and valley diverge from each other due to the growth of the streaks. The difference between the skin frictions at the valley and peak becomes less pronounced when $\hat{x} > 0.16$ due to attenuation of the streaks as is shown in figure 4. The skin friction decreases to attain its minimum value at $\hat{x} \approx 0.37$, and then starts to increase again, signalling that the separation is avoided. Figure 5(*b*) shows the dependence of the separation location $\hat{x}_s$ on the FSVD level ϵ. As ϵ is increased from a very small level, the separation location first shifts upstream but then moves downstream. After passing the minimum distance, $\hat{x}_s$ increases very rapidly with ϵ. Apparently, $\hat{x}_s$ approaches infinite as $\epsilon \to \epsilon_c \approx 0.0040$. In this case, the separation is eliminated. The growth of the fundamental component prompts the forward movement of separation location, whereas the nonlinearly induced mean-flow deformation tends to delay the separation. It is also found that as the adverse pressure
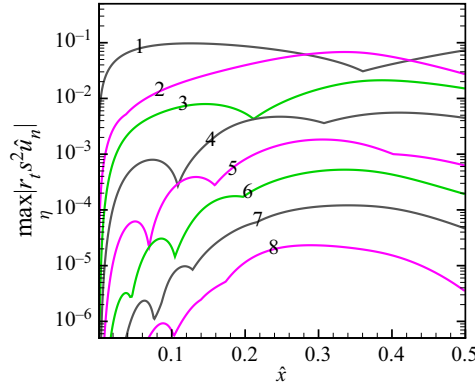
Figure 6. The downstream development of the amplitudes of Fourier modes, $\max_\eta |r_t s^2 \hat{u}_n|$ $(n = 1, 2, \ldots)$ for $d = 0.112$ and $\epsilon = 0.0049$. The parameters are $G_A = 0$ and $R_A = 1145$.

gradient d is increased, the separation location moves forward at a fixed ϵ, and FSVD of a higher intensity are thus required to prevent the separation.

Figure 6 shows the development of $\max_\eta |r_t s^2 \hat{u}_n|$, the maximum amplitude of the fundamental and harmonic components. Note that, unlike the formulation in Xu *et al.* (2020), the mode $(0, 0)$ is no longer present as it is fully absorbed into the steady spanwise-averaged flow in our formulation. Near the leading edge, all harmonics have much smaller amplitudes than that of the fundamental. After the initial non-modal growth, the fundamental mode $(0, 1)$ attenuates starting from $\hat{x} \approx 0.06$ and its amplitude remains almost constant between $\hat{x} = 0.08$ and 0.24, whilst all the harmonics continue to grow overall (but not necessarily monotonically). Among them, mode $(0, 2)$ grows quickly to overtake the fundamental $(0, 1)$ at $\hat{x} \approx 0.28$. As a result, two mushroom structures are anticipated within one spanwise periodic as will be shown later. From $\hat{x} \approx 0.36$, the fundamental mode grows again while all harmonic components attenuate.

It is informative to monitor the streamwise velocity of the distorted boundary layer,

$$U(\eta, z; \hat{x}, \hat{\tau}) \equiv U_B(\hat{x}, \eta) + r_t s^2 \sum_{m,n} \hat{u}_{m,n}(\hat{x}, \eta) \exp(-im\hat{k}_1\hat{\tau} + ink_3 z). \qquad (4.3)$$

In figure 7(*a*), the profiles of U at three spanwise positions are displayed. Near the leading edge, the profiles at different spanwise positions overlap because of the small amplitude of the excited disturbance. As is shown in figure 6, the fundamental mode $(0, 1)$ at $\hat{x} = 0.086$ is the dominant component causing the deficit of the streamwise-velocity profiles at $z = \pi/2$ and π. With the nonlinearly generated $(0, 2)$ mode growing faster, at $\hat{x} = 0.206$ the profile at $z = \pi/2$ almost coincides with that of at $z = \pi$. Eventually at $\hat{x} \geq 0.326$, a larger deficit appears at $z = \pi/2$. Of particular interest is the streamwise-velocity profile at $\hat{x} = \hat{x}_s = 0.356$, the location of the separation which would occur in the absence of FSVD. Now in the presence of FSVD under consideration, flow reversal does not occur at any of these three spanwise positions, indicating that Goldstein's singularity is prevented. The experiment of Simoni *et al.* (2016) found that FSVD of sufficient intensity eliminated separation. Here, we have presented the first theoretical demonstration of this phenomenon. It should be borne in mind that in the nonlinear saturation phase the profiles become highly distorted and as a result may be susceptible to secondary instability. The actual occurrence of bypass transition depends on whether or not secondary instability modes are excited. Our result that separation can be eliminated without resorting to
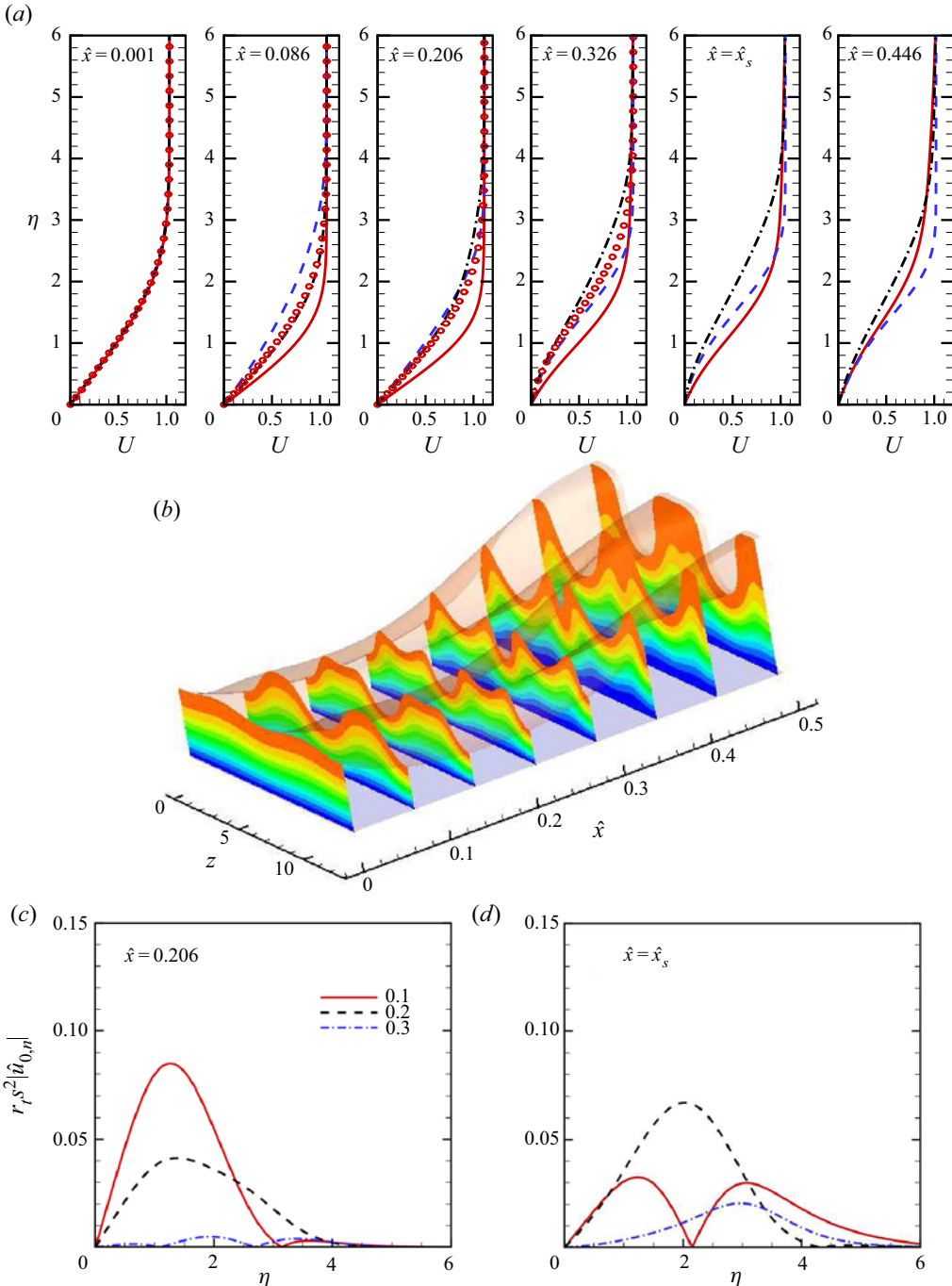
920 A14-22

Figure 7. Streaky boundary layer subject to a favourable-to-adverse pressure gradient with separation being eliminated by FSVD-induced streaks. (*a*) Profiles of the streamwise velocity U at various $\hat{x}$-locations. Solid lines: at the peak ($z = 0$); dashed lines: at the valley ($z = \pi$); dash-dotted lines: at the middle of the peak and valley ($z = \pi/2$); symbols: profiles in the pre-separation region with FSVD being absent. Here, $\hat{x}_s = 0.356$ is the separation location when $\epsilon = 0$. (*b*) The nonlinear evolution of steady streaks illustrated by contours of the streamwise velocity. (*c*,*d*) Streamwise-velocity profiles of fundamental and harmonics $\hat{u}_{0,n}$ at $\hat{x} = 0.206$ and $\hat{x} = \hat{x}_s = 0.356$. The parameters are $G_\Lambda = 0$, $R_\Lambda = 1145$ and $\epsilon = 0.0049$.

920 A14-23
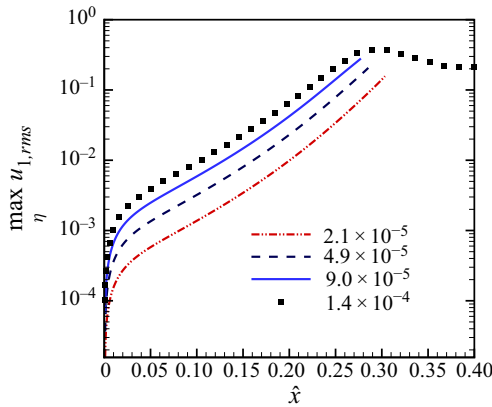
Figure 8. The downstream development of $\max_\eta u_{1,rms}$ for steady Görtler vortices at different ϵ. The parameters are $d = 0.112$, $G_\Lambda = 1501$ and $R_\Lambda = 1145$.

transition suggests a scenario that even if bypass transition does occur, it may not necessarily be the direct or primary cause of separation suppression.

Figure 7(b) presents the evolution and structure of the steady streaks. The spanwise extent displayed is two fundamental wavelengths. Near the leading edge, the streaks resemble those in the case of zero pressure gradient. One streak appears first within a spanwise wavelength, but splits into two streaks as $(0, 1)$ is overtaken by the harmonic $(0, 2)$, whose spanwise wavelength is half of the original one. Two streaks persist for some distances despite the $(0, 1)$ mode becomes dominant again from $\hat{x} \approx 0.41$ as is shown in figure 6, but the structure of one streak would eventually re-emerge farther downstream. Figures 7(c) and 7(d) show the profiles of the fundamental and harmonics in the streamwise velocity at $\hat{x} = 0.206$ and the separation point $\hat{x} = \hat{x}_s = 0.356$ respectively. The fundamental $(0, 1)$ dominates at $\hat{x} = 0.206$, but its magnitude decreases as is indicated in figure 6, and is overtaken by $(0, 2)$ component at $\hat{x} = \hat{x}_s = 0.356$. The $(0, 1)$ mode has two peaks at $\eta \approx 1.3$ and 3.4. These two peaks were also be detected by Martin & Martel (2012) for an elevated initial amplitude of streak shown in their figure 9 (Bottom row). The component $(0, 3)$ acquires a magnitude comparable to that of $(0, 1)$.

4.2. *Concave wall case: Görtler vortices eliminate separation*

In many flows of interest, high-intensity turbulence and streamwise curvature are both present. In this subsection, we investigate how FSVD influences the separation in a curved boundary layer. The slip velocity is the same as equation (4.1) with $d = 0.112$. The Reynolds number is set as $R_\Lambda = 1145$ and the Görtler number $G_\Lambda = 1501$, which are pertinent to an experiment condition of Swearingen & Blackwelder (1987). Figure 8 shows the streamwise development of $u_{1,rms}$ for different FSVD levels. When ϵ is sufficient small, the code 'blows up' in the linear growth stage of the Görtler vortices. The 'blow-up' position moves upstream as ϵ increases. However, when the FSVD level reaches $\epsilon = 1.0 \times 10^{-4}$, 'blow-up' no longer occurs, in which case three stages, non-modal, linear growth and nonlinear saturation, are observed.

Figure 9(a) shows the streamwise development of the skin frictions at the valley and peak. The Görtler vortices excited by FSVD cause the minimum skin friction to occur at $z = \pi$. The streamwise position of the 'blow-up' coincides with the location where the minimum skin friction τ vanishes. As the FSVD level ϵ is increased, the skin friction at
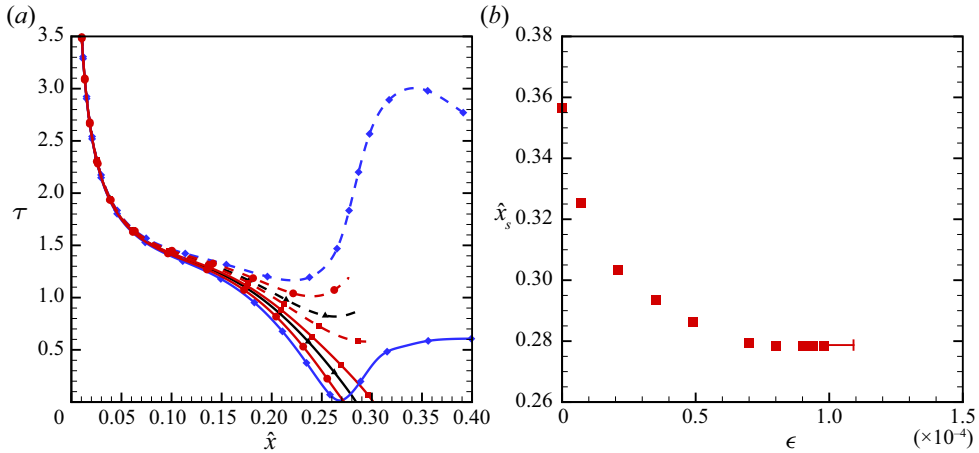
920 A14-24

Figure 9. (*a*) The development of the skin frictions at the peak (dashed lines) and valley (solid lines) at different ϵ. The squares, deltas, circles and diamonds represent the cases of $\epsilon = 2.1 \times 10^{-5}$, 4.9×10^{-5}, 9.0×10^{-5} and 1.4×10^{-4}, respectively. (*b*) The streamwise locations of separation vs FSVD level ϵ for a favourable-to-adverse flow. The error bar indicates uncertainty caused by the limited number of calculations.

the valley decreases very quickly from $\hat{x} \approx 0.1$, and the position at which $\tau = 0$ moves slightly upstream. At $\epsilon = 1.4 \times 10^{-4}$, the skin friction decreases to a positive minimum value at $\hat{x} = 0.27$ and then increases again. Note that separation would occur at $\hat{x} = 0.356$ when $\epsilon = 0$, but in the presence of FSVD, the skin friction at $z = \pi$ remains positive due to the nonlinearly generated mean-flow distortion. Figure 9(*b*) presents the dependence of the separation location $\hat{x}_s$ on ϵ. Unlike the flat-plate case shown in figure 5(*b*), where the separation position shifts to infinity downstream as ϵ approaches a threshold, for the curved wall, with the FSVD intensity increasing, $\hat{x}_s$ shifts upstream monotonically. When the FSVD intensity is low ($\epsilon < 6 \times 10^{-5}$), the upstream shift is rather rapid. However, with further increase of ϵ, the separation location gradually approaches a plateau. The separation no longer occurs when $\epsilon \approx 10^{-4}$. The critical FSVD level to prevent separation is approximately 10^{-4}, much smaller than $\epsilon_c \approx 4 \times 10^{-3}$ in the flat-plate case, indicating that the concave streamwise curvature significantly inhibits the separation for moderate and large values of G_Λ.

The nonlinear interactions generate harmonics. Figure 10 plots the development of the maximum amplitudes of these components. After the initial non-modal growth, the Görtler vortices evolve approximately linearly before reaching saturation at $\hat{x} \approx 0.3$. The fundamental mode $(0, 1)$ is always dominant, and is followed by the nonlinearly generated $(0, 2)$ mode. The behaviour is different from that of the streaks shown in figure 6 for the flat-plate case.

The streamwise-velocity profiles at six streamwise locations are displayed in figure 11(*a*) for the spanwise positions corresponding to $z = 0$ (peak) and $z = \pi$ (valley). The profiles exhibit velocity excess at the peak, while at the valley they feature a deficit. The Görtler vortices grow in height and expand towards the outer edge of the boundary layer, as far as to $\eta \approx 8$. In comparison, over the streamwise range $0.001 \leq \hat{x} \leq 0.446$, the streaks in the flat-plate case only extend up to $\eta \approx 5$ as is shown in figure 7. Special attention is paid to the profiles at $\hat{x} = \hat{x}_s = 0.356$, and no flow reversal is found at either the peak or valley. The separation, which would otherwise occur, is prevented by the Görtler vortices. Figure 11(*b*) presents the evolution and structure of the Görtler vortices.
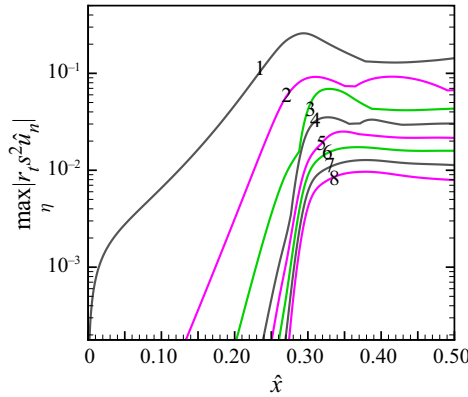
Figure 10. The downstream development of the amplitudes of Fourier modes, $\max_\eta |r_t s^2 \hat{u}_n|$ ($n = 1, 2, \ldots$) for $d = 0.112$ and $\epsilon = 1.4 \times 10^{-4}$. The parameters are $G_\Lambda = 1501$ and $R_\Lambda = 1145$.

The characteristic mushroom-shaped pattern is formed, which is similar to that in the weak adverse-pressure-gradient cases (Xu *et al.* 2020).

4.3. *Boundary layer subject to a persistent adverse pressure gradient*

We now turn to the boundary layer over a flat plate, or concave wall, in an expanding channel, a setting appearing in many experiments (Blair 1992). The inviscid streamwise slip velocity is obtained as (Xu *et al.* 2020)

$$U_e(\hat{x}) = \left(\frac{\sigma_c + 1}{2}\right) + \frac{(\sigma_c - 1)}{2} \frac{\sinh(2r\hat{x})}{\cosh(r\hat{x}) + 1} \quad (r = \pi R_\Lambda \Lambda / a^*). \quad (4.4)$$

The expansion ratio $\sigma_c < 1$ controls the streamwise pressure gradient. Unlike (4.1), the slip velocity (4.4) gives an adverse pressure gradient for all $\hat{x}$ when $\sigma_c < 1$. Figure 12(*a*) plots the variation of the slip velocity. Two rather strong adverse pressure gradients, corresponding to $\sigma_c = 0.63$ and 0.64, are chosen. A no separation case $\sigma_c = 0.65$ is plotted for comparison. Figure 12(*b*) shows the distribution of the skin friction. The separation location moves upstream as the adverse pressure gradient increases.

In the presence of FSVD, the separation location moves as ϵ is varied. Figure 13(*a*) shows the downstream development of $\max_\eta u_{1,rms}$ for the steady Görtler vortices at $\sigma_c = 0.63$ with different ϵ. The separation occurs in the modal growth stage for the two lower levels, $\epsilon = 0.0035$ and 0.0070. At $\epsilon = 0.014$, the separation is eliminated, and nonlinearity influences the evolution of $\max_\eta u_{1,rms}$ even near the leading edge, indicating that nonlinearity plays a decisive role in preventing separation.

At a fixed FSVD level, the centrifugal force due to concave curvature is also an important factor in preventing separation. Figure 13(*b*) displays the downstream development of $\max_\eta u_{1,rms}$ for the steady Görtler vortices at $\sigma_c = 0.63$ with a fixed $\epsilon = 0.014$ but different G_Λ. Three Görtler numbers are chosen for comparison. The evolution of $\max_\eta u_{1,rms}$ overlaps upstream of $\hat{x} = 0.03$, indicating that at the present high FSVD level ($\epsilon = 0.014$), the curvature has little influence on the growth of vortices at the beginning. For the two smaller values of G_Λ, the separation still occurs. Note that the separation takes place in the nonlinear saturation stage of the vortices, which is different from that in the lower FSVD level cases of $\epsilon = 0.007$ and 0.0035 shown in figure 13(*a*). As G_Λ is increased to 1501, the separation is eliminated.
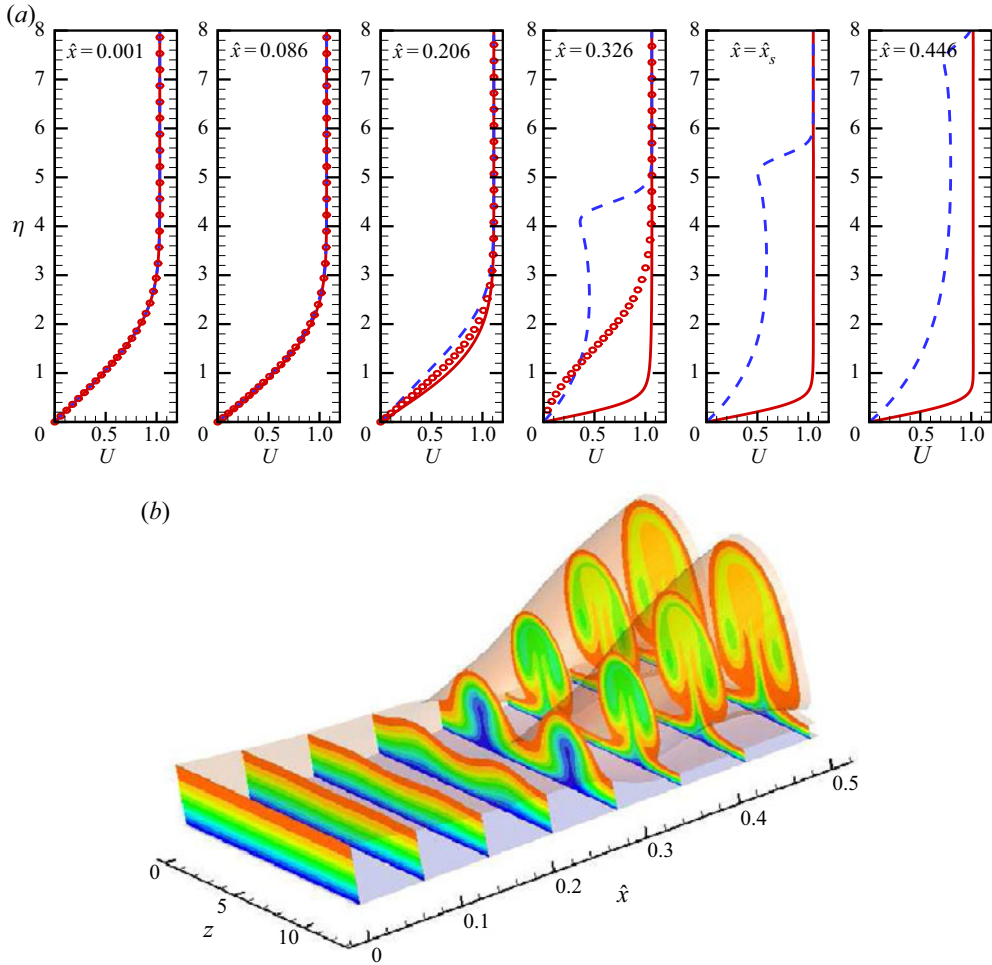
920 A14-26

Figure 11. Boundary layer subject to a favourable-to-adverse pressure gradient with separation being eliminated by FSVD-induced Görtler vortices. (*a*) The profiles of the streamwise velocity U at various $\hat{x}$-locations. Solid lines: at the peak ($z = 0$); dashed lines: at the valley ($z = \pi$); symbols: profiles in the pre-separation region with FSVD being absent. Here, $\hat{x}_s = 0.356$ marks the location of the separation that would occur when $\epsilon = 0$. (*b*) The nonlinear evolution of steady Görtler vortices with $\epsilon = 1.4 \times 10^{-4}$.

Figure 14 displays the evolution of the fundamental and harmonics. The dominant component is the fundamental mode $(0, 1)$. After the non-modal growth, the mode $(0, 1)$ starts to saturate from $\hat{x}_s \approx 0.05$, with the linear growth stage being more-or-less bypassed at such high FSVD level. The separation would occur at $\hat{x} = 0.138$ at $\epsilon = 0$, but disappears in the presence of FSVD with $\epsilon = 0.0175$. Again, the elimination is in the saturation phase of the vortices. The oscillatory behaviour led to halving of the step size $\Delta\hat{x}$, and the comparison shown in figure 14 confirms that the solution is satisfactorily resolved.

Figure 15(*a*) plots the profiles of the streamwise velocity U at various $\hat{x}$-locations. As the Görtler vortices develop, the profile at the valley in the region $\eta < 6$ is highly distorted. These profiles may not be observed in experiments because the amplitude of the secondary instability modes could have grown to a large value. To examine the spanwise characteristics of the steady vortices, we plot the contours of the streamwise velocity at eight streamwise locations in the range of $0.001 < \hat{x} < 0.16$ in figure 15(*b*). The structures
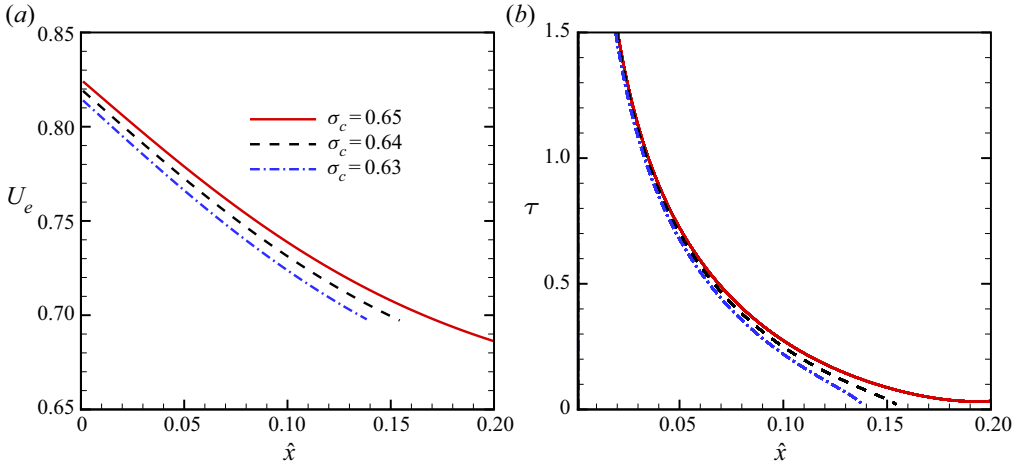
Figure 12. The development of the slip velocity (*a*) and skin friction (*b*) for the separating and non-separating flows when $\epsilon = 0$.
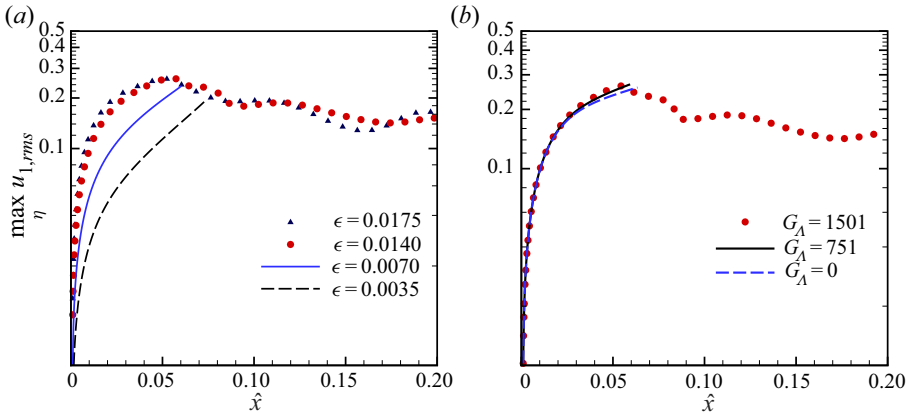

Figure 13. The downstream development of $\max_\eta u_{1,rms}$ for steady Görtler vortices at $\sigma_c = 0.63$ and $R_\Lambda = 1145$. (*a*) Fixed $G_\Lambda = 1501$ with different ϵ. (*b*) Fixed $\epsilon = 0.014$ with different G_Λ.
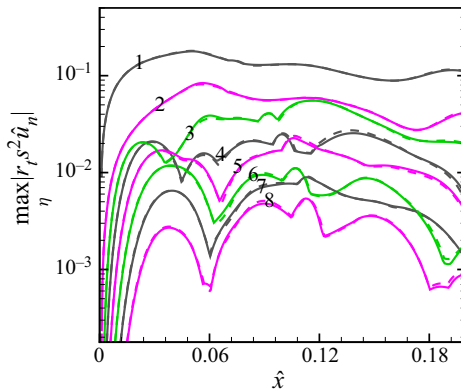

Figure 14. The downstream development of different Fourier components ($n = 1, 2, \ldots, 8$) of the steady Görtler vortices. The parameters are $\epsilon = 0.0175$, $G_\Lambda = 1501$, $R_\Lambda = 1145$ and $\sigma_c = 0.63$. The dashed lines represent the result obtained with the step size $\Delta \hat{x}$ halved.
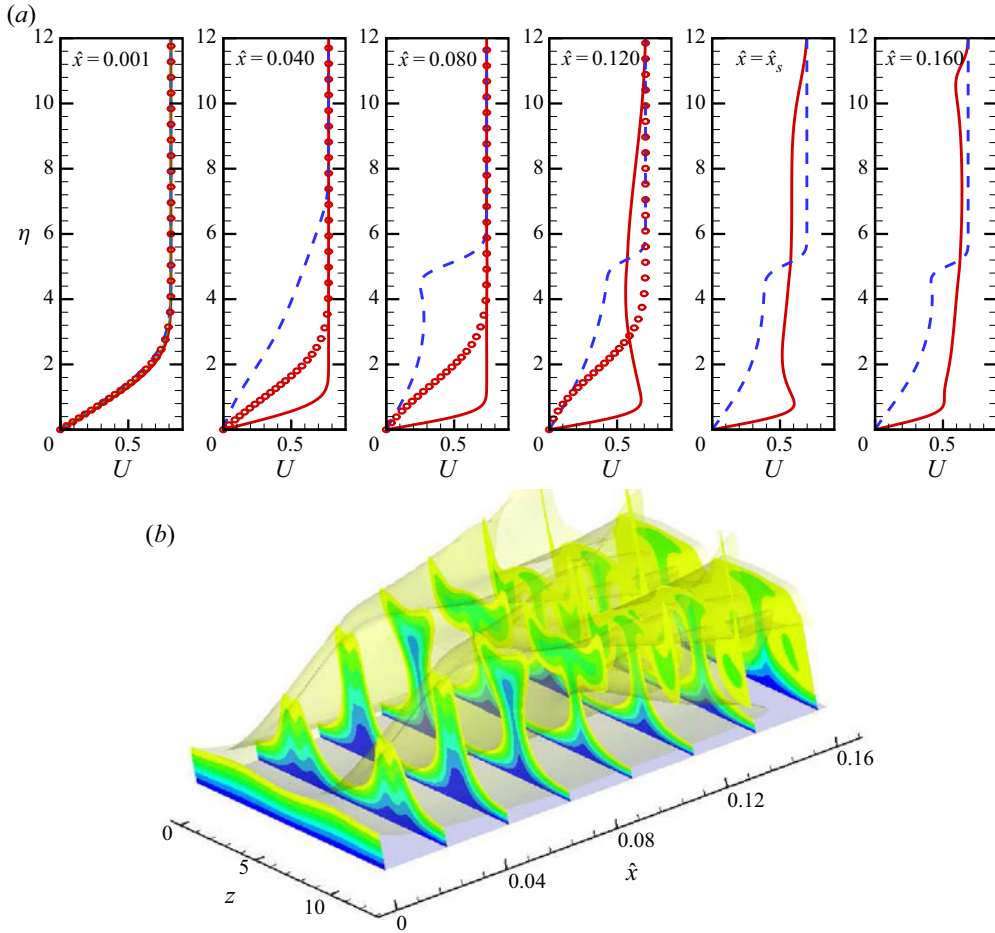
920 A14-28

Figure 15. Boundary layer subject to an adverse pressure gradient but with the separation being eliminated by FSVD-induced Görtler vortices. (*a*) The profiles of the streamwise velocity U at various $\hat{x}$-locations. Solid lines: at the peak ($z = 0$); dashed lines: at the valley ($z = \pi$); symbols: profiles in the pre-separation region with FSVD being absent. Here, $\hat{x}_s = 0.138$ denotes the separation location at $\epsilon = 0$. (*b*) Nonlinear evolution of the steady Görtler vortices. The parameters are $G_\Lambda = 1501$, $R_\Lambda = 1145$ and $\epsilon = 0.0175$.

look rather like the streaks shown in figure 7(*b*). The separation that would otherwise occur at $\hat{x} = \hat{x}_s = 0.138$ is prevented by the saturated Görtler vortices.

Rather extensive calculations are carried out for different ϵ, G_Λ and σ_c in order to map out the dependence of the critical FSVD level ϵ_c on G_Λ and σ_c. The variation of the separation location with ϵ for different G_Λ is displayed in figure 16(*a*). For each fixed G_Λ, increasing ϵ causes the separation location $\hat{x}_s$ to move upstream, until the FSVD level reaches a certain threshold value ϵ_c, for which separation no longer occurs. Figure 16(*b*) shows the variation of ϵ_c with G_Λ. As G_Λ increases, ϵ_c becomes smaller, indicating that concave curvature helps FSVD inhibit the separation.

Figure 17(*a*) shows the variation of the separation location $\hat{x}_s$ with the FSVD level ϵ for different σ_c. For $\sigma_c = 0.7$ and 0.665, the two-dimensional base flow would have not separated when $\epsilon = 0$, however, FSVD of sufficient intensity cause separation because of the linear growth of the Görtler vortices. That an otherwise attached boundary layer separates under the action of free-stream disturbances was demonstrated before for steady
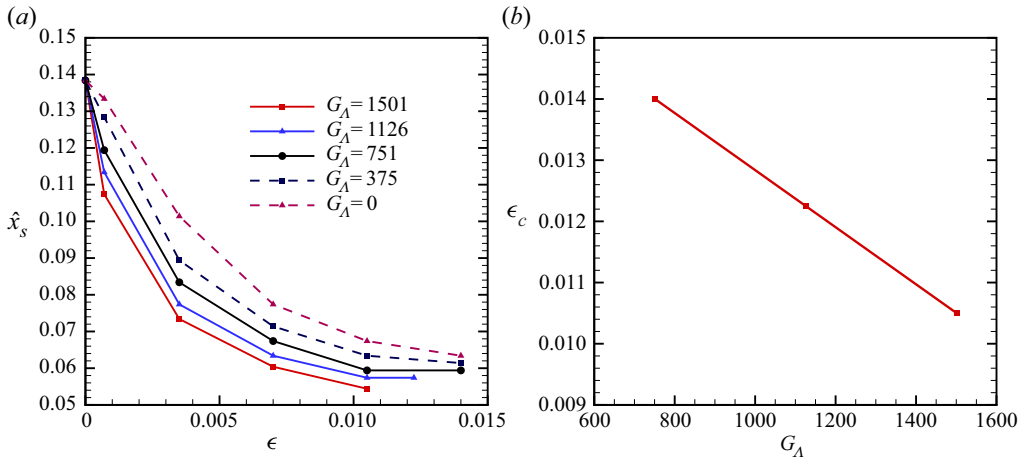
Figure 16. (*a*) The separation location $\hat{x}_s$ vs ϵ for different G_Λ. (*b*) The critical FSVD level ϵ_c vs G_Λ. The parameters are $\sigma_c = 0.63$ and $R_\Lambda = 1145$.
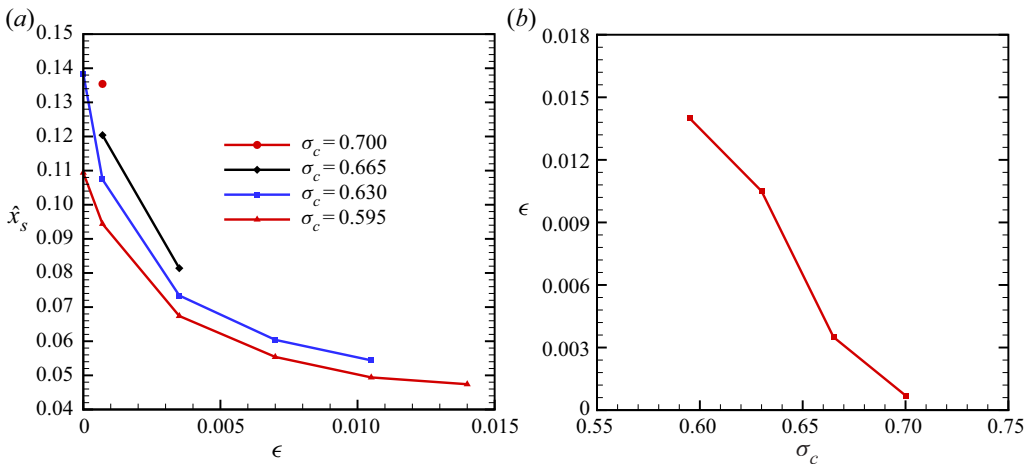

Figure 17. (*a*) The separation location $\hat{x}_s$ vs ϵ for different σ_c. (*b*) The critical FSVD level ϵ_c vs σ_c. The parameters are $G_\Lambda = 1501$ and $R_\Lambda = 1145$.

vorticity normal to the leading edge (Goldstein *et al.* 1992) or in the streamwise direction (Goldstein & Leib 1993). As ϵ is increased, the three-dimensional flow becomes attached again. For $\sigma_c = 0.63$ and 0.595, the boundary layer would separate when $\epsilon = 0$. The separation location moves upstream as ϵ increases until $\epsilon = \epsilon_c$, at which the nonlinear effect becomes significant enough to remove the separation. As figure 17(*b*) indicates, the critical FSVD level ϵ_c for eliminating the separation decreases monotonically with σ_c, suggesting that for a stronger adverse pressure gradient, higher intensity turbulence is required to remove the separation.

4.4. *Unsteady vortices eliminate separation*

We now present results showing how unsteady FSVD eliminate separation. The unsteadiness is characterised by parameter $\hat{k}_1$, which is related to the dimensional
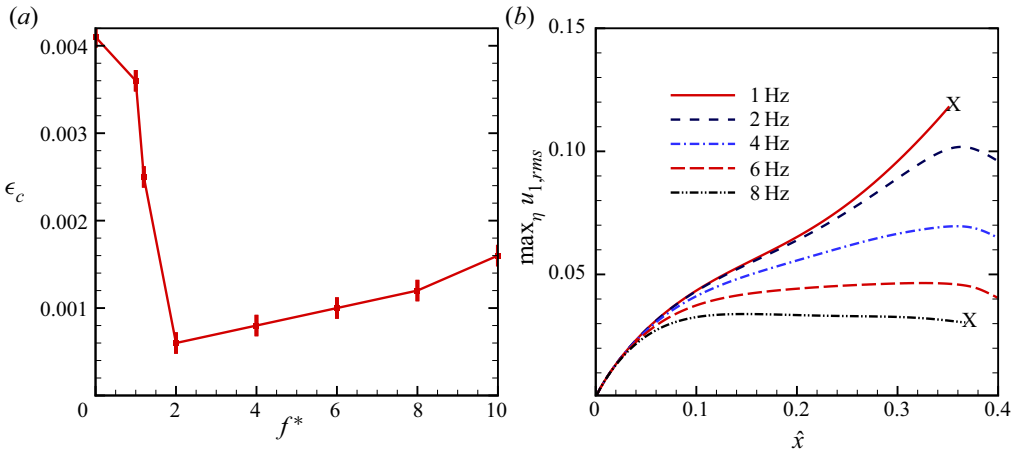
Figure 18. Suppression of separation by unsteady FSVD. (*a*) The critical FSVD level ϵ_c vs the frequency of FSVD for a favourable-to-adverse pressure gradient. The error bars indicate the uncertainty caused by the limited resolution in the search for ϵ_c. (*b*) The downstream development of $\max_\eta u_{1,rms}$ at fixed $\epsilon = 0.001$ for different frequencies. The symbols *x* indicate the separation locations. The parameters are $d = 0.112$, $R_\Lambda = 1145$ and $G_\Lambda = 0$.

frequency f^* via the relation,

$$\hat{k}_1 = R_\Lambda k_1 = 2\pi R_\Lambda f^* \Lambda / U_\infty. \tag{4.5}$$

Calculations are performed for the slip velocity representing a favourable-to-adverse pressure gradient shown in figure 13(*a*). Figure 18(*a*) shows the variation of the critical FSVD level ϵ_c with the dimensional frequency f^*. As the frequency of FSVD increases, ϵ_c reduces dramatically until $f^* \approx 2$ Hz, for which the critical FSVD intensity to remove the separation is the smallest. When $f^* > 2$ Hz, ϵ_c increases slowly with f^* but is still significantly lower than in the steady case. The results suggest that unsteady low-frequency FSVD can be more efficient than steady ones to prevent the separation.

The reason for the existence of an optimal frequency which gives a minimum threshold amplitude to eliminate the separation is due to the competition between the spanwise dependent components and the steady mean-flow distortion (represented by $(0, 0)$ component when an unperturbed base flow can be defined). The latter was found to be more significant than the former in the saturation stage of the streaks (Ricco *et al.* 2011; Xu *et al.* 2020). In order to eliminate the separation, the wall shear must remain positive everywhere along the spanwise direction. The steady spanwise uniform mean-flow distortion acts to increase the wall shear, while the spanwise dependent components, primarily $(1, \pm 1)$ and $(0, 2)$, reduce the wall shear in the valley region. As is shown in figure 19, when unsteadiness (the frequency f^*) is increased first, $(1, \pm 1)$ becomes weaker, and thus the required threshold is reduced. However, with a further increase of f^*, $(0, 2)$ becomes strong and thus the threshold amplitude increases eventually.

Figure 18(*b*) presents the downstream development of $\max_\eta u_{1,rms}$ for the unsteady streaks induced by FSVD of different frequency but with a fixed $\epsilon = 0.001$. The evolution of $\max_\eta u_{1,rms}$ overlaps for different f^* in the region $\hat{x} < 0.05$, indicating that unsteadiness does not play a leading role near the leading edge, as is expected theoretically (Leib *et al.* 1999). When $\hat{x} > 0.05$, the excited unsteady streaks acquire smaller amplitudes for higher frequencies. The separation is prevented for $f^* = 2$, 4 and 6 Hz, but not in the cases of $f^* = 1$ and 8 Hz, since $\epsilon = 0.001$ is below the required threshold as figure 18 indicates.
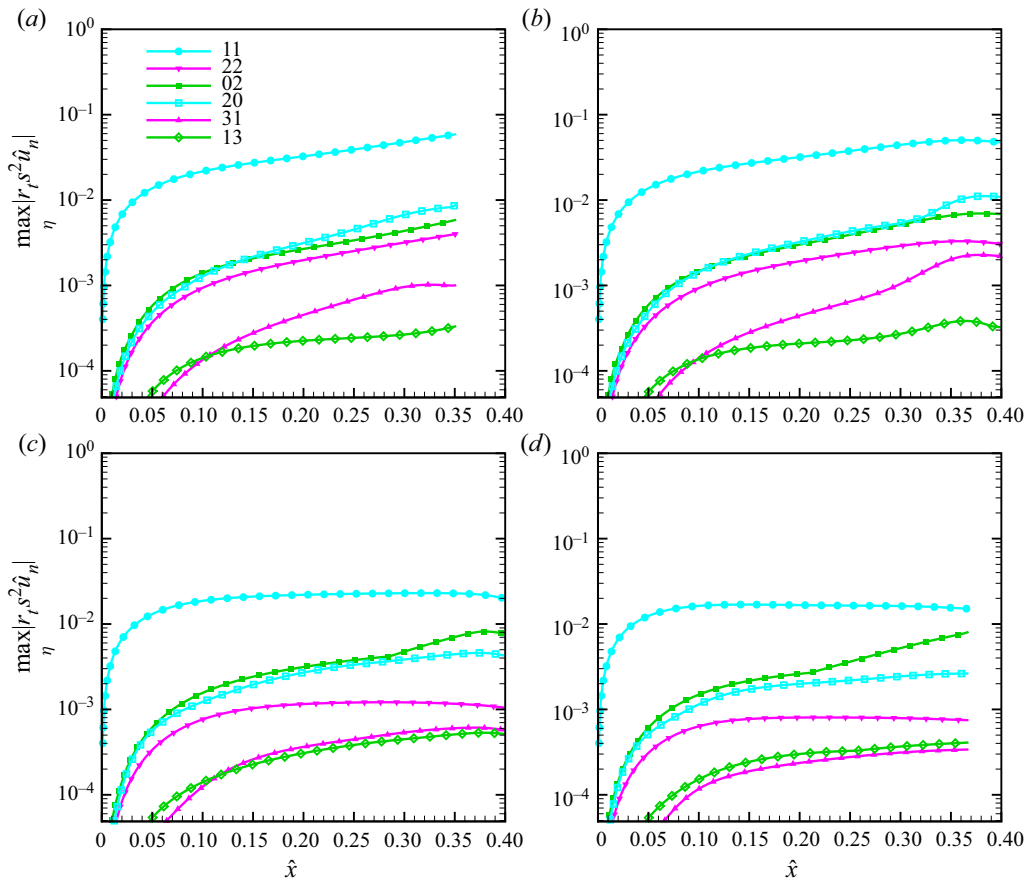
920 A14-31

Figure 19. The downstream development of different Fourier modes for FSVD of different frequencies: (a) $f^* = 1$ Hz, (b) $f^* = 2$ Hz, (c) $f^* = 6$ Hz, (d) $f^* = 8$ Hz. The parameters are $\epsilon = 0.001$, $G_\Lambda = 0$ and $R_\Lambda = 1145$.

That the boundary layer separates again as the frequency $f^* \geq 8$ Hz is due to the reduced amplitude of the excited streaks, failing to reach the required strength to prevent the separation.

It is appropriate at this junction to discuss the relation between the threshold ϵ_c of discrete low-frequency FSVD and the overall FST level required for eliminating separation. This would depend on a number of factors including the spectral property of FST on the one hand, and the geometry, angle of attack and the surface curvature of the aerofoil or turbine blade (the first two of which determine the degree of the adverse pressure gradient) on the other hand. The result presented in figure 18(*a*) suggests that for a typical case of favourable-to-adverse pressure gradient, the threshold level of low-frequency FSVD is only approximately 0.1 % , while experiments indicate that the overall FST level Tu under which a LSB was (almost) completely suppressed was in the range of 1.45 %–5 % (Simoni *et al.* 2016, 2017; Istvan & Yarusevych 2018). The vast difference arises because the FST covers a broadband spectrum of perturbations, the majority of which are trapped in the outer edge of the boundary (Dong & Wu 2013), incapable of penetrating into the boundary layer to impact separation. Only the components in a small low-frequency band are relevant. This suggests that in experimental studies, a Tu restricted to a suitable low-frequency band would need to be introduced to characterise the impact of FST on separation. On the other hand, the theory and calculations need to be extended using a realistic FST model that accounts for a continuum of low-frequency components, as was done in Zhang *et al.* (2011). We expect that the critical intensity in terms of such a Tu would be much lower than the overall FST level.

Figure 19 shows the downstream development of different Fourier components in the streaks excited by FSVD of different frequency. The fundamental mode (1, 1) is dominant in all the four cases. The two-dimensional unsteady harmonic (2, 0) has the second largest amplitude for $f^* = 1$ and 2 Hz, but for $f^* = 6$ and 8 Hz, it is three-dimensional steady component (0, 2) that takes second place. An almost exponential growth of the fundamental mode (1, 1) occurs in the range $\hat{x} = 0.1 \sim 0.35$ for the cases of $f^* = 1$ and 2 Hz, suggesting that a linear low-frequency instability mechanism may be operating at elevated FSVD levels despite the flat plate and an attached boundary layer. It is worth noting that such exponential amplification was observed in experiment (Simoni, Ubaldi & Zunino 2014) and DNS (Hosseinverdi & Fasel 2018). An interesting question is whether this is related to the 'centrifugal instability' (Marxen *et al.* 2009; Marxen & Henningson 2011) that was attributed to $V_{B\hat{x}}$, the streamwise variation of the spanwise-averaged flow. For the present attached boundary layer, the instability is rather weak with a spatial growth rate $\mathrm{d}\ln|\hat{u}_{1,1}|/\mathrm{d}\hat{x} \approx 4$, but could become strong in a separating or separated boundary layer.

The first and second rows of figure 20 displays perspective views of the streamwise-velocity contours in the *y–z* plane at different downstream locations for the unsteady streaks with $f^* = 2$ and 6 Hz. In each case, two phases of time modulation, $\phi \equiv \hat{k}_1\hat{\tau} = 25\pi/16$ and $31\pi/16$, are chosen. At each instant, the streaks look similar to those in the steady cases shown in figure 7(*b*), but the spanwise distribution remains sinusoidal in the late nonlinear stage. The third and fourth rows of figure 20 show the streamwise-velocity profiles of fundamental and harmonics at $\hat{x} = 0.206$ and $\hat{x} = \hat{x}_s$ for unsteady streaks. The (0, 2) mode has two peaks which are the same as shown by Ricco *et al.* (2011) in their figure 5(*a*). For the streaks with frequency $f^* = 2$ Hz, the mode (2, 0) takes the second place. With the frequency increasing to 6 Hz, the inner peak of mode (0, 2) grows to a larger amplitude, leading to that mode (0, 2) overtakes the mode (2, 0) as shown in figure 20(*h*).
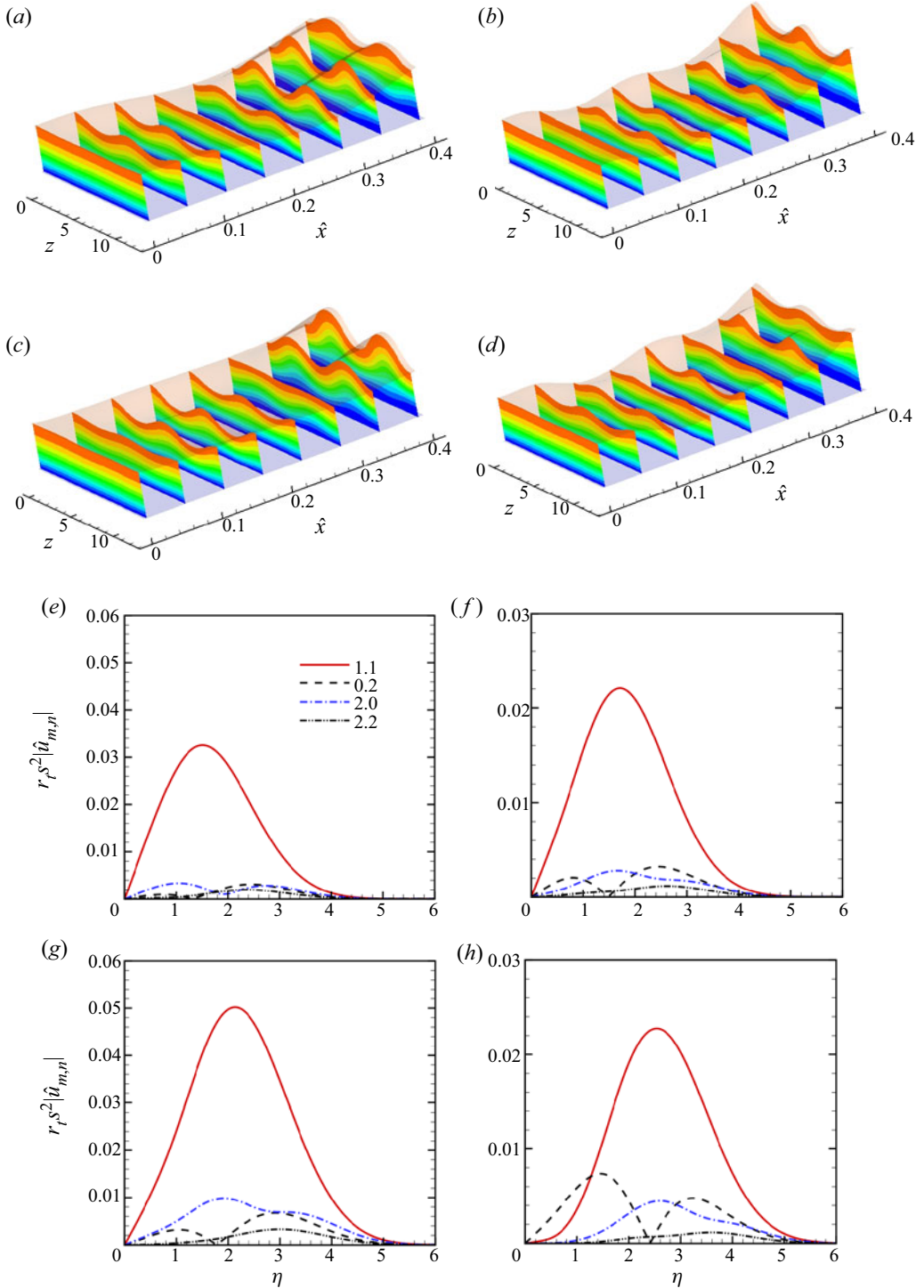
Figure 20. Nonlinear evolution of streaks in a boundary layer where the separation is eliminated by unsteady FSVD with $\hat{k}_1 = 10.54$ (2 Hz, a,c,e,g) and $\hat{k}_1 = 31.61$ (6 Hz, b,d,f,h). First and second rows: contours of the streamwise velocity U at $\phi = 25/16\pi$ and $\phi = 31/16\pi$ respectively. (e–h) The streamwise velocity profiles of fundamental and harmonics at $\hat{x} = 0.206$ and 0.356 respectively. The parameters are $G_\Lambda = 0$, $R_\Lambda = 1145$ and $\epsilon = 0.001$.

920 A14-34

5. Summary and conclusions

A nominally steady two-dimensional boundary layer usually separates when it is subject to an adverse pressure gradient.

It has been shown experimentally that elevated FST of rather moderate level can reduce the size of the separation bubble (O'meara & Mueller 1987; Olson *et al.* 2013; Istvan *et al.* 2017) and even eliminate the separation entirely (Simoni *et al.* 2016, 2017; Zilli *et al.* 2017; Istvan & Yarusevych 2018). This effect of FST was observed in DNS (Wissink & Rodi 2006; McAuliffe & Yaras 2010; Balzer & Fasel 2016). Specifically, the so-called Klebanoff modes (i.e. streaks) induced by low-frequency components in FST play a key role in inhibiting the separation (McAuliffe & Yaras 2010; Hosseinverdi & Fasel 2019). Prompted by these experimental and DNS results, in this paper a theoretical approach was taken to investigate the impact of low-frequency FSVD on separation. The theory is an adoption of that of Xu *et al.* (2020), where a nonlinear initial-boundary-value problem was formulated to describe excitation of streaks and Görtler vortices by FSVD and their evolution. An important part of the formulation was the correct specification of the upstream and far-field conditions which account for quantitatively the action of FSVD on the boundary layer.

In Xu *et al.* (2020), the instantaneous flow is decomposed as the sum of the undisturbed base flow and the perturbation induced by FSVD. This decomposition is not applicable to strong adverse pressure gradients that induce separation because the former part terminates at a finite distance in the form of Goldstein singularity. In order to overcome this obstacle, the flow was split into the steady spanwise-averaged part and the spanwise or time-dependent part. They are nonlinearly coupled, and were computed as a whole numerically. Computations were carried out for two typical forms of slip velocity: one corresponds to a favourable-to-adverse pressure gradient while the other is entirely adverse. With the FSVD level $\epsilon = 0$, these two slip velocities can lead to separation of the two-dimensional boundary layer when the parameter controlling the pressure gradient exceeds a certain threshold. However, if the intensity of FSVD is strong enough, the separation is eliminated. Nonlinearity plays a key role in suppressing the separation, namely, the nonlinear interactions of the spanwise-dependent components generate steady spanwise-independent Reynolds stresses, which drive a mean flow with an enhanced skin friction thereby inhibiting separation. The detailed process leading to separation elimination and the critical FSVD intensity required depend on the form of the adverse pressure gradient and wall curvature. For the favourable-to-adverse pressure gradient and flat-plate case, the separation location first shifts upstream, and then moves downstream quickly with the FSVD intensity increasing from zero. The separation appears to be pushed to infinity as the FSVD level approaches a critical value. The influence of the streamwise curvature on the separation was also investigated in the favourable-to-adverse flow. At the Görtler number $G_\Lambda = 1501$, chosen to represent a typical experimental condition, increasing the FSVD level moves the separation location upstream monotonically. The separation is eliminated when the intensity of FSVD level reaches a critical level, which turns out to be one order of magnitude smaller than that in the flat-plate boundary layer. For an entirely adverse-pressure-gradient flow, the critical FSVD level ϵ_c was found to decrease with G_Λ, suggesting that a concave surface curvature helps inhibit the separation. Calculations performed for different expansion ratio σ_c indicated that ϵ_c increases with the adverse pressure gradient, as might be expected.

We also investigated the effect of unsteady FSVD on the separation. As the frequency of FSVD is increased from zero, the critical FSVD intensity to remove the separation drops quickly to reach a minimum at a low frequency, and it then gradually increases as the frequency is increased further. With a fixed FSVD intensity, the boundary layer responding

to FSVD of a moderate frequency would not separate. However, with further increase of the FSVD frequency, the boundary layer separates again.

By investigating the nonlinear response of boundary layers with adverse streamwise pressure gradients to steady and low-frequency physically realisable FSVD, the present work presented the first theoretical demonstration that FST can eliminate separation by influencing the mean flow directly through the Reynolds stresses. This is a simple mechanism as it does not resort to usual short-wavelength (inviscid Rayleigh or viscous T–S) instability, or transition, and instead the amplification of long-wavelength structures, streaks and Görtler vortices, plays an important role. Our theoretical result is consistent with the earlier experimental finding of Simoni *et al.* (2016) and Simoni *et al.* (2017). The mechanism is probably a fundamental one that operates as well when instability modes or fully turbulent fluctuations are involved, i.e. they influence separation also through the Reynolds stresses and the mean-flow distortion (cf. Marxen & Rist 2010). The present theoretical framework accounts for the receptivity to realisable FSVD, the nonlinear evolution of the resulting streaks or Görtler vortices and the effects of curvature. It may be employed to develop physics-based separation control strategies as well as to assess various means of control in a more physical setting.

As we remarked earlier, when the FSVD intensity $\epsilon < \epsilon_c$ the solutions to the boundary-region equations may not be acceptable because the breakaway separation could exert a long range influence to impact the entire inviscid part of the flow. A further investigation of how FSVD influence a separated boundary layer with a LSB, long or short, is required. This necessitates the inclusion of the simultaneous impact of the LSB on the inviscid outer flow. Our work on this problem is in progress.

Author ORCIDs.

Dongdong Xu https://orcid.org/0000-0001-6886-9157;

Xuesong Wu http://orcid.org/0000-0002-3406-8017.

Appendix A. Newton's iteration solving (3.8*a,b*) and (3.9)

Newton's iteration used to solve (3.8*a,b*) and (3.9) is facilitated by introducing iterations on (F_j^r, U_j^r, G_j^r),

$$(F_j^{(r+1)}, U_j^{(r+1)}, G_j^{(r+1)}) = (F_j^r, U_j^r, G_j^r) + (\delta F_j^{(r)}, \delta U_j^{(r)}, \delta G_j^{(r)}), \tag{A1}$$

where $r = 0, 1, 2, \ldots$. The initial values ($r = 0$) are taken to be those at the previous streamwise station $\hat{x}^{n-1}$. We insert (A1) into (3.8*a,b*) and (3.9), and drop the terms that are quadratic in $\delta F_j^{(r)}$, $\delta U_j^{(r)}$ and $\delta G_j^{(r)}$. This procedure yields the linear system,

$$\delta F_j - \delta F_{j-1} - \frac{\Delta \eta_j}{2}(\delta U_j + \delta U_{j-1}) = r_{1j}, \tag{A2}$$

$$\delta U_j - \delta U_{j-1} - \frac{\Delta \eta_j}{2}(\delta G_j + \delta G_{j-1}) = r_{3j-1}, \tag{A3}$$

$$s_{1j}\delta G_j + s_{2j}\delta G_{j-1} + s_{3j}\delta F_j + s_{4j}\delta F_{j-1} + s_{5j}\delta U_j + s_{6j}\delta U_{j-1} = r_{2j}, \tag{A4}$$

where

$$r_{1j} = F_{j-1}^r - F_j^r + \Delta\eta_j U_{j-1/2}^r, \tag{A5}$$

$$r_{3j-1} = U_{j-1}^r - U_j^r + \Delta\eta_j G_{j-1/2}^r, \tag{A6}$$

$$r_{2j} = R_{j-1/2}^{n-1} - 4\hat{x}^{n-1/2}\frac{Q_{1,j-1/2}^{n-1/2}}{(U_e^2)_{j-1/2}^{n-1/2}} - [\Delta\eta_j^{-1}(G_j^r - G_{j-1}^r) + \alpha_1(FG)_{j-1/2}^r$$

$$- \alpha_2(U^2)_{j-1/2}^r + \alpha^n(G_{j-1/2}^{n-1}F_{j-1/2}^r - F_{j-1/2}^{n-1}G_{j-1/2}^r)]. \tag{A7}$$

The coefficients of the linearised momentum equation (A4) are

$$\left.\begin{array}{c} s_{1j} = \Delta\eta_j^{-1} + \frac{1}{2}(\alpha_1 F_j^r - \alpha^n F_{j-1/2}^{n-1}), \\ s_{2j} = -\Delta\eta_j^{-1} + \frac{1}{2}(\alpha_1 F_{j-1}^r - \alpha^n F_{j-1/2}^{n-1}), \\ s_{3j} = \frac{1}{2}(\alpha_1 G_j^r + \alpha^n G_{j-1/2}^{n-1}), \\ s_{4j} = \frac{1}{2}(\alpha_1 G_{j-1}^r + \alpha^n G_{j-1/2}^{n-1}), \\ s_{5j} = -\alpha_2 U_j^r, \\ s_{6j} = -\alpha_2 U_{j-1}^r. \end{array}\right\} \tag{A8}$$

The boundary conditions (3.13*a,b*) imply that

$$\delta F_0^n = \delta U_0^n = 0, \quad \delta F_J^n = 0. \tag{A9a,b}$$

Let $\boldsymbol{\delta} = [\delta_0, \ \delta_1, \ \cdots, \ \delta_J]^T$ and $\boldsymbol{r} = [r_0, \ r_1, \ \cdots, \ r_J]^T$ with $\delta_j = [\delta F_j, \ \delta U_j, \ \delta G_j]^T$ and $r_j = [r_{1j}, \ r_{2j}, \ r_{3j}]^T$. The linear system (A2)–(A4) and (A9) can be written in a matrix-vector form, $\boldsymbol{A}\boldsymbol{\delta} = \boldsymbol{r}$, where

$$A = \begin{bmatrix} A_0 & C_0 & 0 & 0 & \cdots & 0 & 0 \\ B_1 & A_1 & C_1 & 0 & \cdots & 0 & 0 \\ \cdots & \cdots & \cdots & \cdots & \cdots & \cdots & \cdots \\ 0 & 0 & \cdots & 0 & B_{J-1} & A_{J-1} & C_{J-1} \\ 0 & 0 & \cdots & 0 & 0 & B_J & A_J \end{bmatrix}, \tag{A10}$$

which is the Jacobian matrix of (3.8*a,b*) and (3.9); the matrices A_j, B_j, C_j in (A10) have the non-zero entries as follows:

$$\left.\begin{array}{l} A_0(1,1) = 1; \quad A_0(2,2) = 1; \quad A_0(3,2) = -1, \quad A_0(3,3) = -\Delta\eta_1/2; \\ A_j(1,1) = 1, \quad A_j(1,2) = -\Delta\eta_j/2; \quad A_j(2,1) = s_{3j}, \quad A_j(2,2) = s_{5j}, \\ \quad A_j(2,3) = s_{1j}; \quad A_j(3,2) = -1, \quad A_j(3,3) = -\Delta\eta_{j+1}/2; \\ \quad A_J(1,1) = 1, \quad A_J(1,2) = -\Delta\eta_J/2; \quad A_J(2,1) = s_{3J}, \\ \quad A_J(2,2) = s_{5J}, \quad A_J(2,3) = s_{1J}; \quad A_J(3,2) = 1; \end{array}\right\} \tag{A11}$$

$$\left.\begin{array}{l} B_j(1,1) = -1, \quad B_j(1,2) = -\Delta\eta_j/2; \\ B_j(2,1) = s_{4j}, \quad B_j(2,2) = s_{6j}, \quad B_j(2,3) = s_{2j}; \\ \quad C_j(3,2) = 1, \quad C_j(3,3) = -\Delta\eta_j/2. \end{array}\right\} \tag{A12}$$

Since the matrix A has a block diagonal structure, $\boldsymbol{A}\boldsymbol{\delta} = \boldsymbol{r}$ can be solved by using the block elimination procedure.

Appendix B. Expressions for matrices C_0 and C_1

The non-zero entries of the 6×6 matrix C_0 in (3.18) are

$$
\left.
\begin{aligned}
&C_0(1,4) = 1; \quad C_0(2,1) = -2\mathcal{B}_v, \quad C_0(2,3) = -in, \quad C_0(2,4) = \mathcal{B}_v\eta; \quad C_0(3,6) = 1; \\
&C_0(4,1) = s^2(-im\hat{k}_1 + n^2 k_3^2) + 2\mathcal{B}_v U_B + s^2 U_{B\hat{x}} - \mathcal{B}_v\eta U_{B\eta} + s^2 in k_3 W_B, \\
&\qquad C_0(4,2) = U_{B\eta}, \quad C_0(4,4) = -\mathcal{B}_v\eta U_B + sV_B; \\
&\qquad C_0(5,1) = -s^3 V_{B\hat{x}} + \mathcal{B}_v\eta s V_{B\eta} - 2s^3 G_A \chi_B U_B + 2\mathcal{B}_v s V_B \\
&\qquad\qquad + \mathcal{B}_v\eta s^2(-im\hat{k}_1 + n^2 k_3^2 + in k_3 W_B) + \mathcal{B}_v\eta s^2 U_{B\hat{x}} - \mathcal{B}_v^2\eta^2 U_\eta, \\
&C_0(5,2) = -s^2(-im\hat{k}_1 + n^2 k_3^2) - \mathcal{B}_v U_B - sV_{B\eta} + \mathcal{B}_v\eta U_{B\eta} - s^2 in k_3 W_B, \\
&\qquad C_0(5,3) = (sV_B - \mathcal{B}_v\eta U_B)in, \quad C_0(5,4) = -\mathcal{B}_v, \quad C_0(5,6) = -in; \\
&\qquad C_0(6,1) = (W_{B\hat{x}} s^2 - \mathcal{B}_v\eta W_{B\eta})k_3 s^2, \quad C_0(6,2) = W_{B\eta} k_3 s^2, \\
&\qquad\qquad C_0(6,3) = s^2(-im\hat{k}_1 + n^2 k_3^2 + in k_3 W_B), \\
&\qquad C_0(6,5) = s^2(in k_3^2), \quad C_0(6,6) = sV_B - \mathcal{B}_v\eta U_B,
\end{aligned}
\right\}
$$

(B1)

and those of the matrix C_1 are

$$
\left.
\begin{aligned}
&C_1(2,1) = -s^2; \\
&C_1(4,1) = s^2 U_B; \\
C_1(5,1) = s^3 V_B, \quad &C_1(5,2) = -s^2 U_B, \quad C_1(5,4) = -s^2; \\
&C_1(6,3) = s^2 U_B.
\end{aligned}
\right\}
$$

(B2)

REFERENCES

ALAM, M. & SANDHAM, N.D. 2000 Direct numerical simulation of 'short' laminar separation bubbles with turbulent reattachment. *J. Fluid Mech.* **410**, 1–28.

AVANCI, M.P., RODRÍGUEZ, D. & ALVES, L.S. DE B. 2019 A geometrical criterion for absolute instability in separated boundary layers. *Phys. Fluids* **31** (1), 014103.

BALZER, W. & FASEL, H.F. 2016 Numerical investigation of the role of free-stream turbulence in boundary-layer separation. *J. Fluid Mech.* **801**, 289–321.

BLAIR, M.F. 1992 Boundary-layer transition in accelerating flows with intense freestream turbulence: Part 1. Disturbances upstream of transition onset. *Trans. ASME J. Fluids Engng* **114** (3), 313–321.

CARTER, J.E. & WORNOM, S.F. 1975 Solutions for incompressible separated boundary layers including viscous-inviscid interaction. *NASA Tech. Rep.* SP-347, pp. 125–150.

CEBECI, T. & COUSTEIX, J. 2005 *Modeling and Computation of Boundary-layer Flows: Laminar, Turbulent and Transitional Boundary Layers in Incompressible and Compressible Flows*. Horizons Publishing.

COULL, J.D. & HODSON, H.P. 2011 Unsteady boundary-layer transition in low-pressure turbines. *J. Fluid Mech.* **681**, 370–410.

DIWAN, S.S. & RAMESH, O.N. 2009 On the origin of the inflectional instability of a laminar separation bubble. *J. Fluid Mech.* **629**, 263–298.

DONG, M. & WU, X. 2013 On continuous spectra of the Orr–Sommerfeld/Squire equations and entrainment of free-stream vortical disturbances. *J. Fluid Mech.* **732**, 616–659.

DOVGAL, A.V., KOZLOV, V.V. & MICHALKE, A. 1994 Laminar boundary layer separation: instability and associated phenomena. *Prog. Aerosp. Sci.* **30** (1), 61–94.

DURBIN, P.A. & WU, X. 2007 Transition beneath vortical disturbances. *Annu. Rev. Fluid Mech.* **39**, 107–128.

EMBACHER, M. & FASEL, H.F. 2014 Direct numerical simulations of laminar separation bubbles: investigation of absolute instability and active flow control of transition to turbulence. *J. Fluid Mech.* **747**, 141–185.

GALLAIRE, F., MARQUILLIE, M. & EHRENSTEIN, U. 2007 Three-dimensional transverse instabilities in detached boundary layers. *J. Fluid Mech.* **571**, 221–233.

GASTER, M. 1966 The structure and behaviour of laminar separation bubbles. In *Proc. Conf. AGARD, Rhode-Saint-Genese, Belgium, paper no. 4*, pp. 813–854.

GOLDSTEIN, M.E. 1978 Unsteady vortical and entropic distortions of potential flows round arbitrary obstacles. *J. Fluid Mech.* **89** (03), 433–468.

GOLDSTEIN, M.E. & DURBIN, P.A. 1980 The effect of finite turbulence spatial scale on the amplification of turbulence by a contracting stream. *J. Fluid Mech.* **98** (03), 473–508.

GOLDSTEIN, M.E. & LEIB, S.J. 1993 Three-dimensional boundary-layer instability and separation induced by small-amplitude streamwise vorticity in the upstream flow. *J. Fluid Mech.* **246**, 21–41.

GOLDSTEIN, M.E., LEIB, S.J. & COWLEY, S.J. 1992 Distortion of a flat-plate boundary layer by free-stream vorticity normal to the plate. *J. Fluid Mech.* **237**, 231–260.

GOLDSTEIN, S. 1948 On laminar boundary-layer flow near a position of separation. *Q. J. Mech. Appl. Maths* **1** (1), 43–69.

GROSCH, C.E. & SALWEN, H. 1978 The continuous spectrum of the Orr–Sommerfeld equation. Part 1. the spectrum and the eigenfunctions. *J. Fluid Mech.* **87** (1), 33–54.

HÄGGMARK, C.P., BAKCHINOV, A.A. & ALFREDSSON, P.H. 2000 Experiments on a two-dimensional laminar separation bubble. *Phil. Trans. R. Soc. Lond.* A **358** (1777), 3193–3205.

HALL, P. 1988 The nonlinear development of Görtler vortices in growing boundary layers. *J. Fluid Mech.* **193**, 243–266.

HAMMOND, D.A. & REDEKOPP, L.G. 1998 Local and global instability properties of separation bubbles. *Euro. J. Mech.* B*/Fluids* **17** (2), 145–164.

HERBERT, T. 1997 Parabolized stability equations. *Annu. Rev. Fluid Mech.* **29** (1), 245–283.

HOSSEINVERDI, S. & FASEL, H.F. 2018 Role of Klebanoff modes in active flow control of separation: direct numerical simulations. *J. Fluid Mech.* **850**, 954–983.

HOSSEINVERDI, S. & FASEL, H.F. 2019 Numerical investigation of laminar–turbulent transition in laminar separation bubbles: the effect of free-stream turbulence. *J. Fluid Mech.* **858**, 714–759.

HSIAO, C.T. & PAULEY, L.L. 1994 Comparison of the triple-deck theory, interactive boundary layer method, and Navier–Stokes computation for marginal separation. *Trans. ASME J. Fluids Engng* **116**, 22–28.

ISTVAN, M.S., KURELEK, J.W. & YARUSEVYCH, S. 2017 Turbulence intensity effects on laminar separation bubbles formed over an airfoil. *AIAA J.* **56** (4), 1335–1347.

ISTVAN, M.S. & YARUSEVYCH, S. 2018 Effects of free-stream turbulence intensity on transition in a laminar separation bubble formed over an airfoil. *Exp. Fluids* **59** (3), 52.

JACOBS, R.G. & DURBIN, P.A. 2001 Simulations of bypass transition. *J. Fluid Mech.* **428**, 185–212.

JONES, L.E., SANDBERG, R.D. & SANDHAM, N.D. 2008 Direct numerical simulations of forced and unforced separation bubbles on an airfoil at incidence. *J. Fluid Mech.* **602**, 175–207.

KALTER, M. & FERNHOLZ, H.H. 2001 The reduction and elimination of a closed separation region by free-stream turbulence. *J. Fluid Mech.* **446**, 271–308.

KARP, M. & HACK, M.J.P. 2020 Optimal suppression of a separation bubble in a laminar boundary layer. *J. Fluid Mech.* **892**, A23.

KIM, J., MOIN, P. & MOSER, R. 1987 Turbulence statistics in fully developed channel flow at low Reynolds number. *J. Fluid Mech.* **177**, 133–166.

KURELEK, J.W., LAMBERT, A.R. & YARUSEVYCH, S. 2016 Coherent structures in the transition process of a laminar separation bubble. *AIAA J.* **54** (8), 2295–2309.

LEIB, S.J., WUNDROW, D.W. & GOLDSTEIN, M.E. 1999 Effect of free-stream turbulence and other vortical disturbances on a laminar boundary layer. *J. Fluid Mech.* **380**, 169–203.

MALIK, M.R. 1990 Numerical methods for hypersonic boundary layer stability. *J. Comput. Phys.* **86** (2), 376–413.

MARENSI, E., RICCO, P. & WU, X. 2017 Nonlinear unsteady streaks engendered by the interaction of free-stream vorticity with a compressible boundary layer. *J. Fluid Mech.* **817**, 80–121.

MARTIN, J.A. & MARTEL, C. 2012 Nonlinear streak computation using boundary region equations. *Fluid Dyn. Res.* **44** (4), 045503.

MARXEN, O. & HENNINGSON, D.S. 2011 The effect of small-amplitude convective disturbances on the size and bursting of a laminar separation bubble. *J. Fluid Mech.* **671**, 1–33.

MARXEN, O., LANG, M. & RIST, U. 2012 Discrete linear local eigenmodes in a separating laminar boundary layer. *J. Fluid Mech.* **711**, 1–26.

MARXEN, O., LANG, M. & RIST, U. 2013 Vortex formation and vortex breakup in a laminar separation bubble. *J. Fluid Mech.* **728**, 58–90.

MARXEN, O., LANG, M., RIST, U., LEVIN, O. & HENNINGSON, D.S. 2009 Mechanisms for spatial steady three-dimensional disturbance growth in a non-parallel and separating boundary layer. *J. Fluid Mech.* **634**, 165–189.

MARXEN, O., LANG, M., RIST, U. & WAGNER, S. 2003 A combined experimental/numerical study of unsteady phenomena in a laminar separation bubble. *Flow Turbul. Combust.* **71** (1), 133–146.

MARXEN, O. & RIST, U. 2010 Mean flow deformation in a laminar separation bubble: separation and stability characteristics. *J. Fluid Mech.* **660**, 37–54.

MARXEN, O., RIST, U. & WAGNER, S. 2004 Effect of spanwise-modulated disturbances on transition in a separated boundary layer. *AIAA J.* **42** (5), 937–944.

MCAULIFFE, B.R. & YARAS, M.I. 2010 Transition mechanisms in separation bubbles under low-and elevated-freestream turbulence. *Trans. ASME J. Turbomach.* **132** (1), 011004.

MICHELIS, T, YARUSEVYCH, S. & KOTSONIS, M. 2017 Response of a laminar separation bubble to impulsive forcing. *J. Fluid Mech.* **820**, 633–666.

MICHELIS, T., YARUSEVYCH, S. & KOTSONIS, M. 2018 On the origin of spanwise vortex deformations in laminar separation bubbles. *J. Fluid Mech.* **841**, 81–108.

OLSON, D.A., KATZ, A.W., NAGUIB, A.M., KOOCHESFAHANI, M.M., RIZZETTA, D.P. & VISBAL, M.R. 2013 On the challenges in experimental characterization of flow separation over airfoils at low Reynolds number. *Exp. Fluids* **54** (2), 1470.

O'MEARA, M.M. & MUELLER, T.J. 1987 Laminar separation bubble characteristics on an airfoil at low Reynolds numbers. *AIAA J.* **25** (8), 1033–1041.

OWEN, P.R. & KLANFER, L. 1953 On the laminar boundary layer separation from the leading edge of a thin aerofoil. *Tech. Rep.* CP 220. Royal Aircraft Establishment, UK.

PRANDTL, L. 1904 Über flussigkeitsbewegung bei sehr kleiner reibung. In *Verh. III, Intern. Math. Kongr., Heidelberg*, pp. 484–491. Teubner.

RICCO, P., LUO, J. & WU, X. 2011 Evolution and instability of unsteady nonlinear streaks generated by free-stream vortical disturbances. *J. Fluid Mech.* **677**, 1–38.

RIST, U. & AUGUSTIN, K. 2006 Control of laminar separation bubbles using instability waves. *AIAA J.* **44** (10), 2217–2223.

RIST, U. & MAUCHER, U. 2002 Investigations of time-growing instabilities in laminar separation bubbles. *Eur. J. Mech.* B/*Fluids* **21** (5), 495–509.

RODRÍGUEZ, D., GENNARO, E.M. & JUNIPER, M.P. 2013 The two classes of primary modal instability in laminar separation bubbles. *J. Fluid Mech.* **734**, R4.

RODRÍGUEZ, D., GENNARO, E.M. & SOUZA, L.F. 2021 Self-excited primary and secondary instability of laminar separation bubbles. *J. Fluid Mech.* **906**, A13.

RODRÍGUEZ, D. & THEOFILIS, V. 2010 Structural changes of laminar separation bubbles induced by global linear instability. *J. Fluid Mech.* **655**, 280–305.

RUBAN, A.I. 1981 Singular solution of boundary layer equations which can be extended continuously through the point of zero surface friction. *Fluid Dyn.* **16** (6), 835–843.

RUBAN, A.I. 1982 Asymptotic theory of short separation regions on the leading edge of a slender airfoil. *Fluid Dyn.* **17** (1), 33–41.

SERVINI, P., SMITH, F.T. & ROTHMAYER, A.P. 2017 The impact of static and dynamic roughness elements on flow separation. *J. Fluid Mech.* **830**, 35–62.

SERVINI, P., SMITH, F.T. & ROTHMAYER, A.P. 2018 The impact of dynamic roughness elements on marginally separated boundary layers. *J. Fluid Mech.* **855**, 351–370.

SIMONI, D., LENGANI, D., UBALDI, M., ZUNINO, P. & DELLACASAGRANDE, M. 2017 Inspection of the dynamic properties of laminar separation bubbles: free-stream turbulence intensity effects for different Reynolds numbers. *Exp. Fluids* **58**, 66.

SIMONI, D., UBALDI, M. & ZUNINO, P. 2014 Experimental investigation of flow instabilities in a laminar separation bubble. *J. Therm. Sci.* **23** (3), 203–214.

SIMONI, D., UBALDI, M., ZUNINO, P. & AMPELLIO, E. 2016 Free-stream turbulence effects on the boundary layer of a high-lift low-pressure-turbine blade. *J. Therm. Sci.* **25** (3), 195–206.

STEWARTSON, K. 1970 Is the singularity at separation removable? *J. Fluid Mech.* **44** (2), 347–364.

STEWARTSON, K., SMITH, F.T. & KAUPS, K. 1982 Marginal separation. *Stud. Appl. Maths* **67** (1), 45–61.

SWEARINGEN, J.D. & BLACKWELDER, R.F. 1987 The growth and breakdown of streamwise vortices in the presence of a wall. *J. Fluid Mech.* **182**, 255–290.

SYCHEV, V.V. 1972 Laminar separation. *Fluid Dyn.* **7** (3), 407–417.

TANI, I. 1964 Low-speed flows involving bubble separations. *Prog. Aerosp. Sci.* **5**, 70–103.

THEOFILIS, V., HEIN, S. & DALLMANN, U. 2000 On the origins of unsteadiness and three-dimensionality in a laminar separation bubble. *Phil. Trans. R. Soc. Lond.* A **358** (1777), 3229–3246.

VELDMAN, A.E.P. 1981 New, quasi-simultaneous method to calculate interacting boundary layers. *AIAA J.* **19** (1), 79–85.

WATMUFF, J.H. 1999 Evolution of a wave packet into vortex loops in a laminar separation bubble. *J. Fluid Mech.* **397**, 119–169.

WISSINK, J.G. & RODI, W. 2006 Direct numerical simulations of transitional flow in turbomachinery. *ASME J. Turbomach.* **128** (4), 668–678.

Wu, X. & Dong, M. 2016 Entrainment of short-wavelength free-stream vortical disturbances in compressible and incompressible boundary layers. *J. Fluid Mech.* **797**, 683–728.

Wu, X., Zhao, D. & Luo, J. 2011 Excitation of steady and unsteady Görtler vortices by free-stream vortical disturbances. *J. Fluid Mech.* **682**, 66–100.

Wundrow, D.W. & Goldstein, M.E. 2001 Effect on a laminar boundary layer of small-amplitude streamwise vorticity in the upstream flow. *J. Fluid Mech.* **426**, 229–262.

Xu, D. 2020 Receptivity, instability and separation of boundary layer over a curved surface subject to elevated free-stream vortical disturbances. PhD thesis, Tianjin University.

Xu, D., Liu, J. & Wu, X. 2020 Görtler vortices and streaks in boundary layer subject to pressure gradient: excitation by free-stream vortical disturbances, nonlinear evolution and secondary instability. *J. Fluid Mech.* **900**, A15.

Xu, D., Zhang, Y. & Wu, X. 2017 Nonlinear evolution and secondary instability of steady and unsteady Görtler vortices induced by free-stream vortical disturbances. *J. Fluid Mech.* **829**, 681–730.

Yarusevych, S. & Kotsonis, M. 2017 Steady and transient response of a laminar separation bubble to controlled disturbances. *J. Fluid Mech.* **813**, 955–990.

Zhang, Y., Zaki, T., Sherwin, S. & Wu, X. 2011 Nonlinear response of a laminar boundary layer to isotropic and spanwise localized free-stream turbulence. *AIAA Paper* 2011-3292.

Zilli, J., Sutton, D.M. & Lavoie, P. 2017 Effect of freestream turbulence on laminar separation bubbles and flow transition on an SD7003 airfoil at low Reynolds numbers. *AIAA Paper* 2017-0302.